Thesis

Influence of the proteasome inhibitor bortezomib on cell cycle distribution of human synovial sarcoma cells

An experimental analysis

Submitted by

Philip Gams

For the degree of

Doctor medicinae universiae
(Dr. med. univ.)

At the

Medical University of Graz (AUT)

Performed at

Department of Orthopedics and Trauma Surgery

Supervised by

Priv.-Doz.^{in} Mag.^{a} rer.nat. Dr.^{in} scient.med. Birgit Lohberger

Graz, November 10, 2017

Declaration

I hereby declare that I have authored this thesis independently, that I have not used other than the declared sources or resources, and that I have explicitly marked all material which has been quoted either literally or by content from the used sources.

Graz, November 10, 2017 *Philip Gams eh*

Acknowledgement

I am particularly grateful to my supervisor Dr. Birgit Lohberger for the valuable guidance as well as for her encouragement and patience during the whole course of this study. Furthermore, I am much indebted for the valuable information, the practical support and guidance of Heike Kaltenegger and Nicole Stündl.

Among the numerous friends who supported me, I would especially like to thank Monica Klamminger for English-language proof reading.

I also want to express my very profound gratitude to my parents Karin and Walter who supported me in every possible way to complete my studies successfully.

Finally, I would like to express my sincere appreciation to my girlfriend Viktoria for the invaluable moral support and for standing by me in all situations.

Abstract

A synovial sarcoma is an aggressive malignant tumor with a pronounced tendency for local recurrence and metastasis. With an incidence of 2-4/100000 it represents the fourth most common malignant soft tissue tumor and occurs, with an average disease age of 35 years, preferably in younger patients. The use of chemotherapeutic agents, often only shows moderate success and is limited by side effects. The currently poor prognosis is based on the usually late diagnosis position on the one hand and on the limited therapeutic possibilities on the other. Therefore, it is essential to find new, more effective substances to enhance the therapeutic options and to improve the prognosis of the patients.

The drug bortezomib from the substance class of proteasome inhibitors may represent such a substance. The current approval is limited to a few specific, malignant haematological disorders. However, numerous studies have already demonstrated an antineoplastic effect even on solid tumors. The effects of bortezomib on synovial sarcoma cells are still widely unexplored.

In this study, it is clearly shown that Bortezomib inhibits, depending on the concentration, the proliferation rate, the growth behavior as well as the viability of synovial carcinoma cells (SW-982).
Based on collected flow cytometry data, cell accumulation was observed in G2-phase. The measured results lead to the conclusion that bortezomib drives synovial carcinoma cells into a G2/M arrest.
The expression of certain genes under the influence of bortezomib was determined by rt-qPCR. At a concentration of 10 nM (IC50), a statistically significant decrease of CDK2 was detected after 48 hours.

The collected data indicates that bortezomib can also express its anti-carcinogenic effect in synovial sarcoma cells. Further the study shows that bortezomib has the requirements to complement future therapies. Overall more information must be generated and therefore further *in-vitro* and *in-vivo* studies are needed to examine the effect of bortezomib in more detail.

Zusammenfassung

Das Synovialsarkom ist ein aggressiver maligner Tumor mit einer ausgeprägten Neigung zur Lokalrezidiv und Metastasenbildung. Mit einer Inzidenz von 2-4/100000 stellt es den vierthäufigsten malignen Weichgewebstumor dar und tritt, mit einem mittleren Erkrankungsalter von 35 Jahren, bevorzugt bei jüngeren Patienten auf. Der Einsatz von Chemotherapeutika zeigt häufig nur mäßigen Erfolg und ist durch die dosislimitierenden Nebenwirkungen nur eingeschränkt möglich. Die derzeit noch schlechte Prognose beruht einerseits auf der meist späten Diagnosestellung und andererseits auf den begrenzten therapeutischen Möglichkeiten. Daher ist es essentiell, neue, effektivere Substanzen zu finden um die therapeutischen Optionen auszubauen und die Prognose der Patienten zu verbessern.

Der Arzneistoff Bortezomib, aus der Wirkstoffklasse der Proteasom-Inhibitoren, stellt möglicherweise eine solche Substanz dar. Die aktuelle Zulassung beschränkt sich auf den Einsatz bei wenigen bestimmten, malignen hämatologischen Erkrankungen. In zahlreichen Studien konnte bereits ein antineoplastischer Effekt auf solide Tumore nachgewiesen werden. Die Auswirkungen von Bortezomib auf Synovialsarkomzellen sind dagegen noch weitgehend unerforscht.

In dieser Arbeit konnte mittels MTS-Cell Viability Assay und xCELLigence RD System eindeutig gezeigt werden, dass Bortezomib die Proliferationsrate bzw. das Wachstumsverhalten sowie die Lebensfähigkeit von Synovialsarkomzellen (SW-982), in Abhängigkeit von der verwendeten Konzentration, hemmt.
Auf Basis der erhobenen Durchflusszytometrie Daten wurde eine Zellakkumulation in der G2-Phase beobachtet woraus sich Schlussfolgern lässt, dass Bortezomib die Synovialsarkomzellen in einen G2/M Arrest führt.
Die Expression bestimmter Gene, unter dem Einfluss von Bortezomib, wurde mittels rt-qPCR eruiert. Hier zeigte sich bei einer Konzentration von 10 nM (IC50) eine statistisch signifikante Abnahme von CDK2 nach 48 Stunden.

Die erhobenen Daten veranschaulichen, dass Bortezomib seine antikarzinogene Wirkung auch bei Synovialsarkomzellen entfaltet und möglicherweise zukünftige Therapieschemen ergänzen könnte. Hierzu sind jedoch noch weitere *in-vitro* und *in-vivo* Studien nötig.

Contents

Abbreviation

Cdc25c	Cell Division Cycle 25C
CDKs	Cyclin-dependent kinases
cDNA	Complementary deoxyribonucleic acid
CC	Cell Cycle
CCM	Cell culture medium
DAPI	4′,6-Diamidin-2-phenylindol
DNA	Deoxyribonucleic acid
dsDNA	Double stranded deoxyribonucleic acid
EFS	Event-free survival
FLS	Fibroblast-like synoviocytes
M	Mitosis
MFS	Metastasis-free survival
MTS	3-(4,5-dimethylthiazol-2-yl)-5-(3-carboxymethoxyphenyl)-2-(4-sulfophenyl)-2H-tetrazolium, inner salt
NADH	Nicotinamide adenine dinucleotide
NADPH	Nicotinamide adenine dinucleotide phosphate
PCR	Polymerase chain reaction
RIN	RNA integrity number
RNA	Ribonucleic acid
rpm	Rounds per minute
rt	Room temperature
RT-qPCR	Real-time quantitative polymerase chain reaction
SAC	Spindle assembly checkpoint
SD	Standard deviation
ssDNA	Single stranded deoxyribonucleic acid
STR	Short tandem repeats
TRIS HCL	Tris(hydroxymethyl) aminomethane hydrochloride

Index of Figures

Index of Tables

1 Introduction

1.1 Synovial sarcoma

The synovial sarcoma (SS) is one of the most common malign soft tissue tumors (STT). It is an aggressive neoplasm of mesenchymal origin [5]. The term "synovial sarcoma" is rooted in clinical everyday life. This designation however can be misleading because it is neither developed within the synovium, nor is it structured like the normal synovia. In fact, the term SS is based on morphological similarity to the synovia in embryonic development [2,3].

1.1.1 Epidemiology

SS is the fourth most commonly occurring soft tissue tumor. It comprises approximately 10% of all soft tissue tumors. Most frequently it occurs in the adolescent and young adult population (median age 35) [1,4]. With an incidence of two to four new cases per 100,000 inhabitants, STT only accounts for about 1% of all malign neoplasms in Germany [15]. Some authors described a slight male predominance (1.2:1 ratio) [5], others have not indicated a predilection for one sex [6]. Moreover, there are no different incidences in relation to certain races or ethnic groups reported [1].

1.1.2 Histopathology

Three histologic main subtypes are distinguished: poorly differentiated, monophasic, and biphasic SS. Depending on the mitotic activity and the extent of tumor necrosis, SSs are stratified into grade 2 (intermediate) and grade 3 (high grade) lesions [8]. Intermediate graded SSs show an improved metastasis- and disease-free survival rate. Apart from disease stage, the histologic grade is the most important prognostic factor [9].

Poorly differentiated SS:

This subtype occurs in 15%–25% of all lesions. In general, poorly differentiated synovial sarcomas are high-grade tumors. Typical is a high mitotic activity, an epithelioid morphology and tumor necrosis. The epithelioid growth pattern is composed of densely packed, relatively uniform small ovoid cells (Figure 1) [1,7].

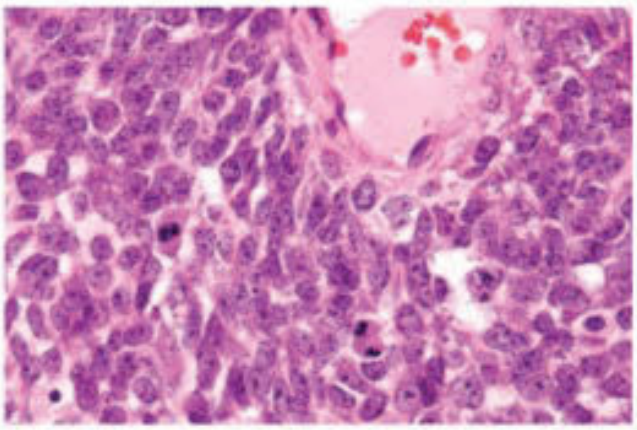

Figure 1. Photomicrographs of a poorly differentiated synovial sarcoma
Poorly differentiated SS have a characteristic epithelioid growth pattern and small, densely packed, ovoid cells (original magnification, 250×). Source adapted from: [1].

Monophasic SS:

Monophasic synovial sarcoma is the most common subtype and represents approximately 50%–60% of all cases of SSs. This subtype has a predominant mesenchymal spindle cell component and a moderate mitotic activity. The cells have ovoid, pale colored nuclei with small nucleoli (Figure 2). Monophasic SS is usually stratified as an intermediate-grade sarcoma but it can also appear as a high-grade lesion [1,7]. This subtype is associated with a poor prognosis for metastasis-free survival [9].

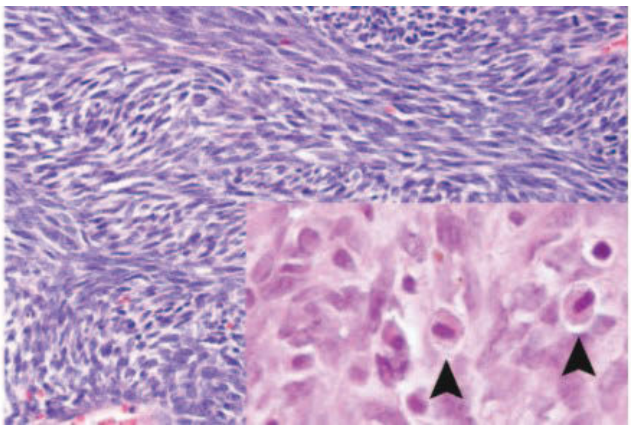

Figure 2. Photomicrographs of a monophasic synovial sarcoma
Predominance of mesenchymal spindle cells characterizes monophasic SS (original magnification, 200×; inset magnification, 400×). The monophasic subtype typically appears with obvious mast cells (arrowheads). Source adapted from: [1].

Biphasic SS:

Biphasic synovial sarcoma represents 20%–30% of all SSs. This subtype includes both an epithelial as well as a mesenchymal spindle cell component in variable compositions (Figure 3). Usually the epithelial cells form glandular structures but they may also appear in a papillary, nest/chord-shaped or in a solid way. Biphasic SSs are, like the monophasic SSs, mostly intermediate-grade lesions. However, they can also emerge as a high grade tumor [1,10].

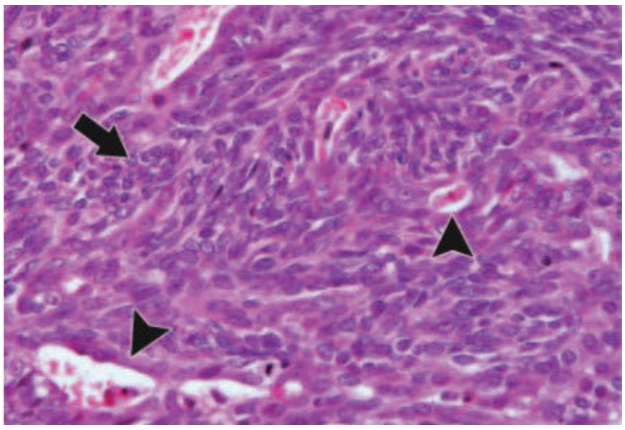

Figure 3. Photomicrographs of a biphasic synovial sarcoma
The biphasic synovial sarcoma typically appears with (mesenchymal) spindle cell component (arrow) and (epithelial) glandular structures (arrowheads) (original magnification, 250×). Source adapted from: [1].

1.1.3 Clinical Features

Contrary to what the term SS suggests, they are not associated with normal synovial tissue and they hardly ever arise within the joint. Approximately 80% of all primary SSs occur in the extremity (60%– 71% lower extremity). They preferably arise in paraarticular regions and grows in connection to tendons, bursae, and joint capsules [10]. The most common site of involvement is the knee, especially the popliteal fossa. Non-extremity manifestations like the trunk, retroperitoneal, abdominal, head or neck are also possible [1, 11].

A slowly progressive, palpable swelling is typical for SSs. Patients often report pain which can precede the clinically recognizable space-occupying lesion. Movement restrictions of neighboring joints as well as b-symptomatic (unexplained fever, massive night sweat and unwanted weight loss of more than 10% of body weight within six months) are usually rare [1, 7, 11]. Due to the mild, non-specific clinical symptoms it takes an average period of 2-4 years to pose the correct diagnosis [12].

1.1.4 Treatment and Prognosis

Local control of SSs is primarily achieved by a wide, “en bloc” resection with tumor negative resection margins. A complicating factor can be that SSs often appears close to neurovascular structures and large joints. Therefore, a radical surgical excision often causes functional disorders. In cases where a complete gross resection is not feasible, an amputation and/or a disarticulation is unavoidable [13].

To improve the local control and to reduce local recurrences, radiotherapy can be offered complementary. Preoperative radiotherapy should be initiated if the surgeon presumes that negative resection margins are not feasible. Postoperative radiotherapy should be conducted if the resection margins are positive. The greatest noticeable impact shows radiotherapy if the SS is only marginally resected. [11,13]. In a retrospective analysis Ferrari, Gronchi, Casanova and colleagues showed a 5-year local-recurrence-free survival rate of 57.4% for patients who received postoperative irradiation (after a marginal resection) whereas the survival rate was only 7.1% for those who did not undergo radiation therapy [11]. However, if the SS is completely resected, a statistically significant overall survival due to radiotherapy is not reported [1, 13].

Relating to adjuvant chemotherapy different trials are non-conclusive. Some have shown a limited survival benefit. Overall, the response rate is only moderate (approximately 50%) [13]. In general, however, it can be asserted that chemotherapy achieves particularly high event-free survival (EFS) and metastasis-free survival (MFS) rates for young patients with small tumors [12, 13]. Furthermore, there could be shown that adjuvant chemotherapy significantly improves the 5-year EFS rate for patients who had completely removed SS (measuring < 5cm). Apart from this, neoadjuvant chemotherapy can also be beneficial for patients. A recently published study explored that neoadjuvant chemotherapy is effective against distant metastasis and improves the overall survival time [14].

Currently, the most effective substances are Doxorubicin and high-dose Ifosfamide. In addition to the substances mentioned, Trabectedin and Pazopanib are also proved beneficial. Figure 4 shows the current therapy algorithm for advanced SSs [16].

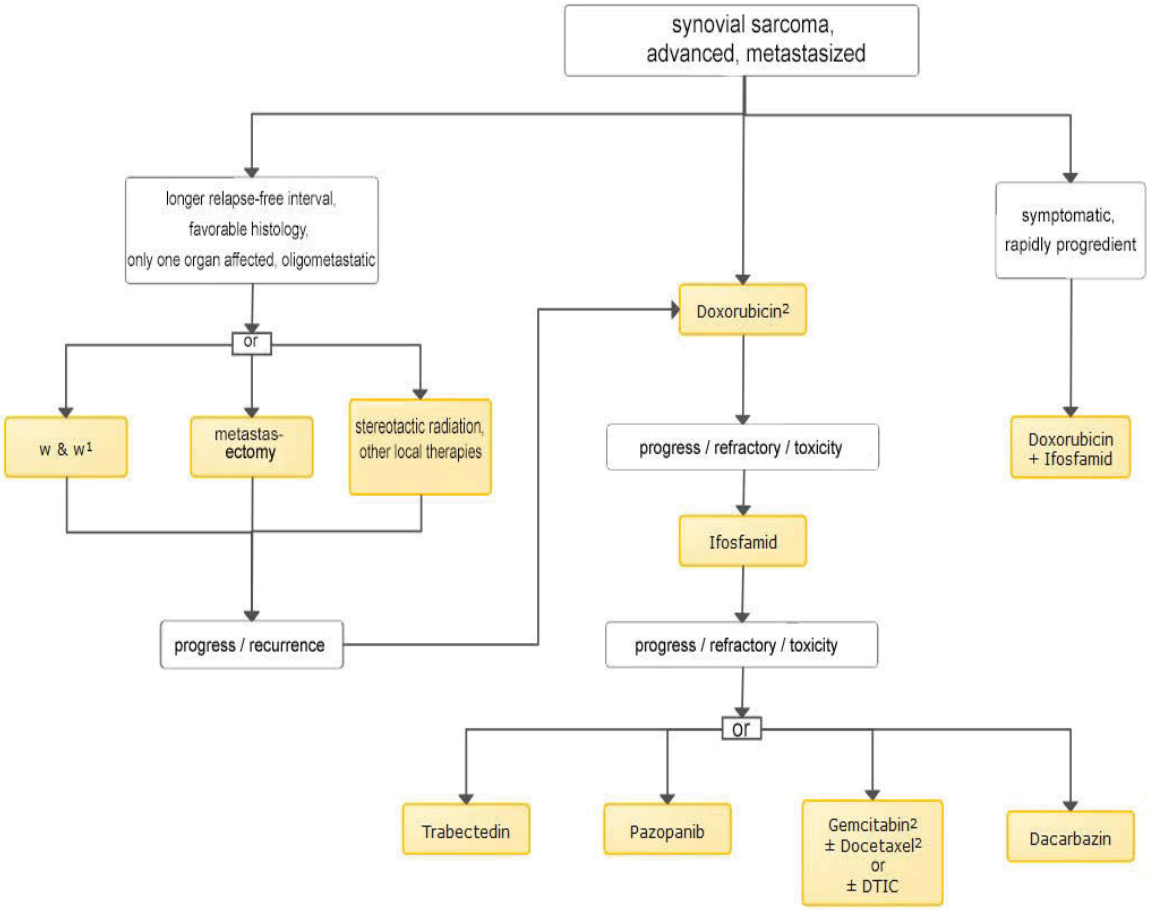

Figure 4. Therapy algorithm for advanced synovial sarcoma (original version in German)
[1] w & w– watch and wait; [2] the combination with Olaratumub is approved, but the importance is unclear; Source adapted from: [16].

SSs highly tend to form metastases (in about 41%) and local recurrences (in about 30-50%). Approximately 16% of all patients have distant metastases on initial diagnosis [15]. Generally, the major part of the metastases occurs in the first 2-5 years after treatment. Most of them are located in the lung (94% of cases) followed by lymph nodes (4%- 8% of cases) [1].

By combining chemo- and local therapy, patients with an intermediate or high-grade SS, have a 5-year survival rate ranging from 36%-76%. The 10-year survival rate is currently between 20% and 63% [1, 10, 11].

The above-mentioned facts or rather the low response rate and poor prognosis for SS-patients show, that there is a clear requirement for less toxic and more effective chemotherapies.

1.2 Cell Cycle

The cell cycle (CC) describes the life of a cell from origin, throughout lifetime, until division in two daughter cells. The CC originally consists of two consecutive fundamentally different processes called mitosis and interphase (Figure 5) [17, 18].

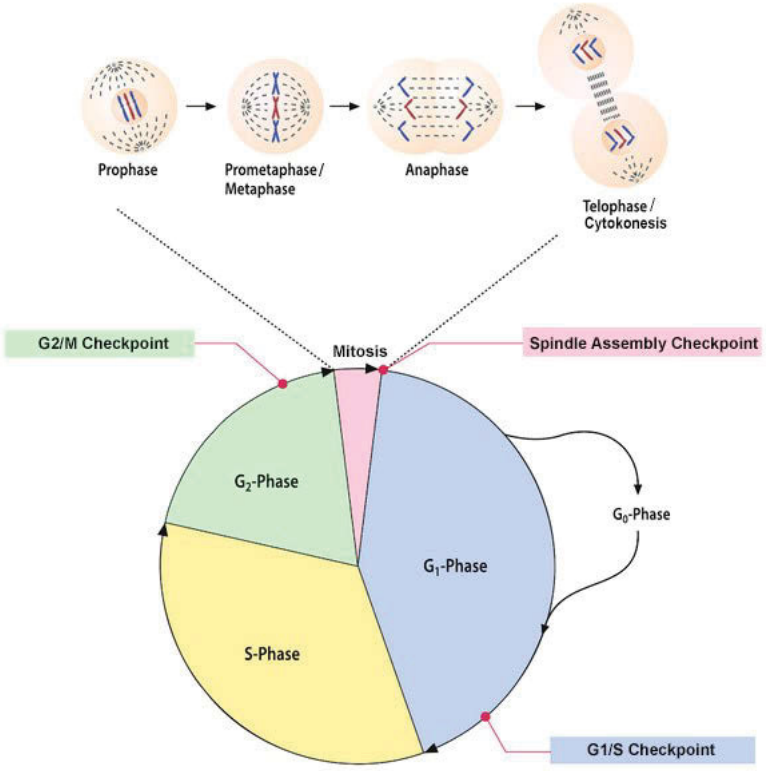

Figure 5. The individual phases of the cell cycle including three substantial checkpoints. (original version in German) Source adapted from: [20]

According to the cell-morphology, mitosis is divided into various stages which aims to produce two identical daughter cells and ensure that each of these cells receives an equal complement of the genome [19]. Figure 5 shows the main stages of mitosis called prophase, metaphase, anaphase, and telophase.

Basically, in the interphase the cells are growing, replicating its DNA and accumulating nutrients to prepare themselves for mitosis. Interphase includes the G1- (gap-1), S- (synthesis) and G2- (gap-2) phase (Figure 5). The replication of DNA only occurs in the S-phase.

Furthermore, there is a resting state called G0-phase. Non-proliferative or non-growing cells often enter the G0-stage and may remain in this stage for a long time (possibly indefinitely). And also the cellular senescence, which is caused by DNA damage or degeneration, can navigate the cells into G0-phase. Growth factor inhibition is another factor that drives cells into this phase [18, 21].

1.2.1 Regulation and Checkpoints

Cells are driven through CC by cyclin-dependent kinases (CDKs) which are activated by cyclins. The term cyclin refers to the fact that most of them are synthesized and destroyed in a cyclical way during the CC (except cyclin D). Contrary to cyclins, CDK proteins are not expressed periodically [18]. So far, nine CDKs have been identified but only four of them are directly involved in navigating the CC. These four are divided in three interphase CDKs comprising CDK2, CDK4 and CDK6 as well as one mitotic CDK named CDK1 [18,22]. Until now, ten cyclins have been described. They are assigned to four different classes: The A-, B-, D- and E-cyclins [23].

To recognise possible errors during chromosome segregation and DNA synthesis, checkpoints observe the proper progression. Basically, an activation of these checkpoints arrests the cell cycle through modulation of CDKs. Halting the process provides time to handle stress and repair DNA defects, before re-entering or permanently leaving the CC [18, 22, 23]. Three main checkpoints are distinguished (Figure 5).

G1/S checkpoint (restriction point):

This checkpoint regulates the transition from G1 to S phase and is defined as a point of no return. At the restriction point, cell cycle arrest can be induced by inhibition of growth factors or DNA damage. DNA damage can cause a high level of P53 activity which results in CDK inhibition and CC arrest. After passing G1/S checkpoint, the cell cycle progression is independent from growth factors [18].

G2/M checkpoint:

The G2/M checkpoint is positioned after DNA replication and prevents cells from initiating mitosis when they progress into G2-phase with damaged or unrepaired DNA [24].

Spindle assembly checkpoint (SAC):

The SAC controls the proper chromosome segregation through modulating the CDK1 activity and stops, if necessary, the cell cycle in metaphase. A defective spindle assembly checkpoint may lead to accumulation of numerical chromosomal aberrations [23].

To pass the restriction point, the most complex regulated checkpoint, D-type cyclins (encoded by the CCNB1 gene) bind and activate CDK4 as well as CDK6 to form the cyclin D/CDK4/6-kinase complex (Figure 6). As already mentioned, D cyclins are not subjected to any cyclical fluctuations. For stimulating the D cyclin synthesis, a sufficient amount of growth factors is necessary [18, 24]. During G1-phase, the cyclin D/CDK4/6-kinase complex gradually phosphorylates and partially inactivates pocket proteins, especially the RB (retinoblastoma) protein [24, 25]. At the end of G1-phase, the cyclin E/CDK2-kinase complex further phosphorylates these pocket proteins, which ultimately result in their complete inactivation (Figure7). Afterwards, the inactivation leads to the release of the transcription factors E2F-1 and DP-1, which activates the transcription of their associated genes. The arising gene-products are required for the currently starting S-phase [18, 24, 25].

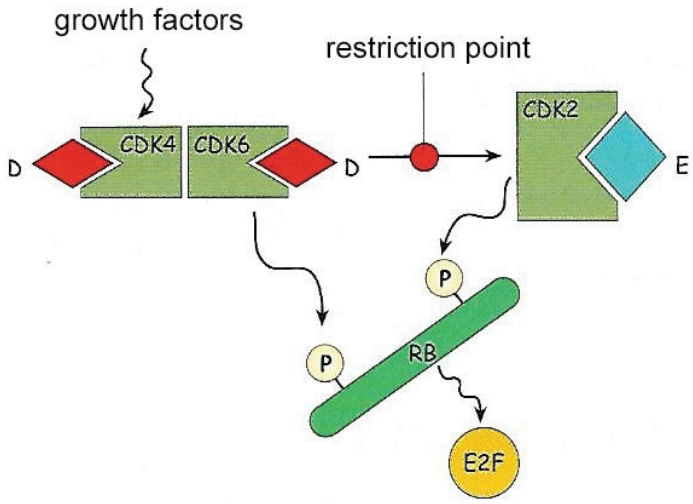

Figure 6. Restriction point and G1-phase cyclins.
The phosphorylated RB protein releases the transcription factor E2F. Source adapted from: [26]

During the late S-phase, cyclin A binds and activates CDK2. The resulting cyclin A/CDK2-kinase complex leads to a nuclear envelope breakdown and facilitates the transition to the G2-phase. Following the degradation of A cyclins, the mitosis-promoting activity from the currently formed cyclin B/CDK1-kinase complex, drives the cells through mitosis (Figure 7) [18, 24].

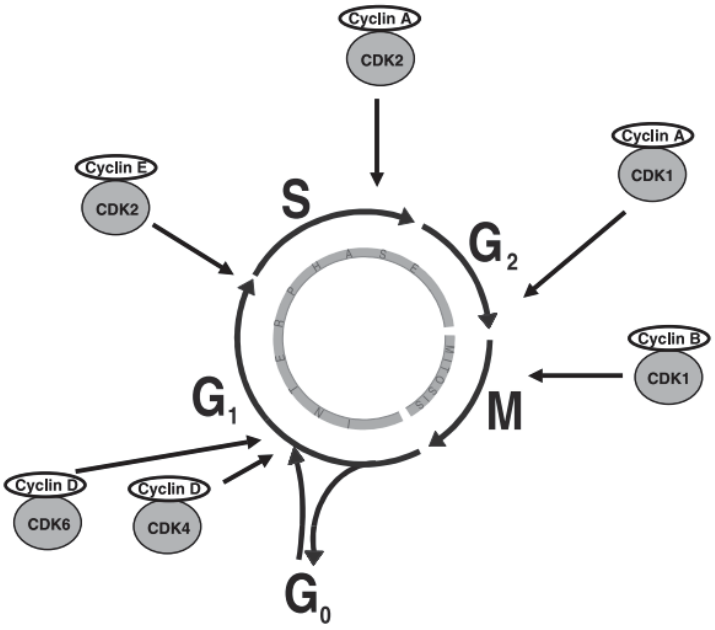

Figure 7. Sequence of the cell cycle.
Cyclins can interact with different CDKs and CDKs with different cyclins. Source adapted from: [18]

1.2.2 DNA damage response

In response to DNA damage, many molecular pathways are activated to prevent cells from processing cell cycle and replicating defective DNA. These pathways result in a significant inhibition of the cell division cycle protein 25c (Cdc25), in an increase of p16 and/or in an increase of the p53 level [23, 29]. There are much more regulating proteins, but to describe all of them would go beyond the scope of this paper.

Cdc25:

The Cdc25 phosphatase regulates the activation of CDK by dephosphorylation of amino acids. To activate the Cyclin B/Cdk1-kinase complex and to progress through CC, the dephosphorylation by Cdc25 at both inhibitory amino acids, tyrosine 15 and threonine 14, at CDK 1, is required [18, 26].

Cdc25 degradation delays the transition to S-phase and causes a G1 arrest for a few hours. A prolongated G1 arrest is achievable by a p53-dependent mechanism [24].

The deregulation or overexpression of Cdc25 is often associated with neoplastic formations [18].

P16:

The p16 major task is the inhabitation of CDK4 and CDK6 caused by the competitive displacement of cyclin D. This process avoids the phosphorylation of the RB protein and further the release of the transcription factor E2F. These happenings prevent the cell from entering S phase [18, 28].

An altered p16 leads to an unrestricted progress through G-phase. RB protein, cyclin D/CDK 4/6-kinase complex and p16 are functionally interconnected. In almost every kind of human cancer alterations of at least one of these regulators can be found [18].

P53:

Under normal conditions, the p53 level is very low and does not exert any influence on the CC progression. However, under certain conditions such as DNA damage or hypoxia (Figure 8), the p53 level can be increased rapidly. Under the mentioned requirements, p53 gets phosphorylated, which avoids the ability of MDM2 to engage it. This mechanism prevents p53 from proteasomal degradation. The stabilized and activated p53 can lead to a wealth of cellular outcomes, pre-eminently p21-gene mediated CC arrest (especially at G1/S or G2/M) and BAX-gene mediated apoptosis [18, 29].

Owing to the pivotal role in protecting the genomic integrity, p53 is also known as the "guardian of the genome" [29].

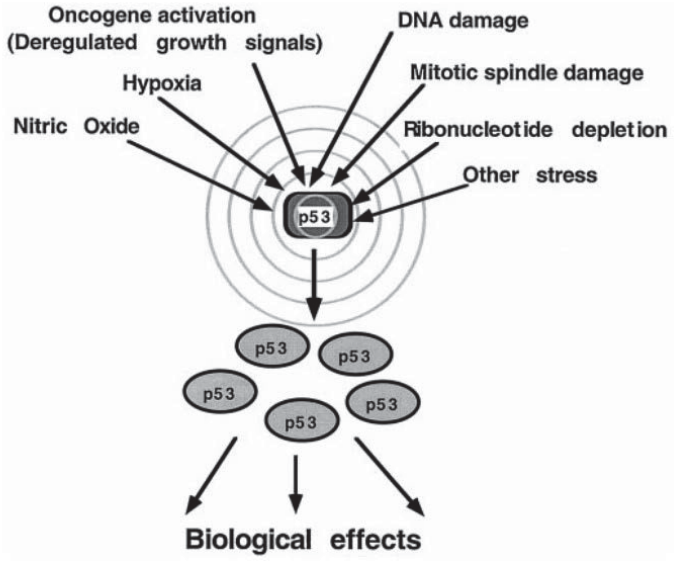

Figure 8. P53-the "guardian of the genome"
Conditions which lead to an increase of p53 level. Source adapted from: [29]

1.2.3 The role of proteasomes

Protein degradation is essential for the cellular function as well as for the proper progress through CC. In eukaryotes, the ubiquitin-proteasome system (UPS) mainly accomplishes the protein degradation. In this context substrates, which were supposed to be eliminated, are tagged with ubiquitin. The eukaryote 26s proteasome is a compound of the 19s and the 20s subcomplexes. The regulatory 19s particle can recognize ubiquitinated substrates in order to subsequently translocate them into the 20s particle, which represents the proteolytic part of the proteasome (Figure 9) [30, 31].

To guarantee a proper cellular performance, cyclins and CDK complexes induce their own proteasome-dependent degradation [18]. Another key role, in relation to the cellular survival, plays the already mentioned proteasome-dependent degradation of MDM2 bonded p53 [29].

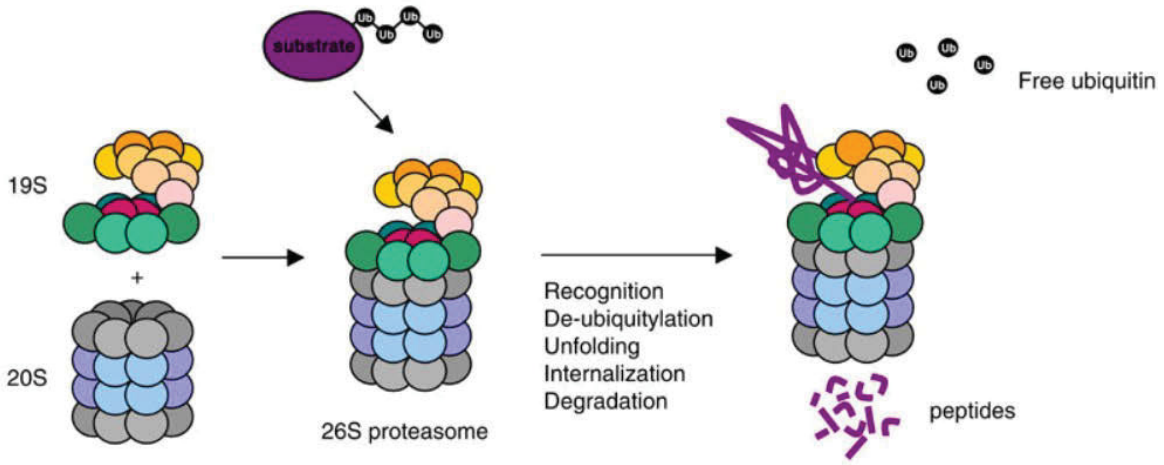

Figure 9. The 26S proteasome and the ubiquitylated substrate.
Both subcomplexes (20s core and 19s lid particle) are forming the 26s proteasome. The regulatory 19s particle is able to recognize, deubiquitylate, unfold, and translocate substrates into the catalytic centre of the core particle. Source adapted from: [32]

1.3 Bortezomib

The proteasome inhibitor Bortezomib is the first in its class and works by blocking the function of the eukaryote 26s proteasomes [34]. The inhibition of proteasomes interrupts the proteolysis and as a consequence a variety of signal cascades. Bortezomib stabilizes p53, p27, p21, Bax, and IκBα. IκBα is a negative regulator of the nuclear transcription factor κB (NF-κB) which plays a major role in tumor proliferation, metastasis, angiogenesis and in promoting chemoresistance. Bortezomib abates the NF-κB activity

which notably results in an enhanced treatment response [36]. Furthermore, especially in cancer cells, the inhibition of proteasomes leads to accumulation of pro-apoptotic proteins, which causes CC stagnation and ultimately cell death [33, 39]. Consequently, it is easily comprehensible that proteasome inhibition is a target for cancer therapy. Therefore, substances such as bortezomib play a central role in many considerations in relation to new therapies [33].

So far, bortezomib is approved for the treatment of multiple myeloma and mantle cell lymphoma [35]. Several clinical trials showed that the treatment with bortezomib (in single- or combination therapy) leads to a significant survival benefit for these patients [33, 36]. Moreover, bortezomib was and is subject of numerous clinical trials. These trials have also proved its antitumor activity in other haematological malignancies as well as in several solid tumors, including prostate cancer, lung carcinoma, colon cancer, ovarian cancer, and breast cancer [36–38]. Kao C. and his colleagues found out that bortezomib blocks the autophagic activity in various cancers and disestablishes the chemotherapy-related autophagy [37]. This synergistic cytotoxic effect may help to develop new combination therapies for several cancers.

1.4 Study objectives

Currently, bortezomib plays an important role in treatment of haematological malignancies and many trials on several cancerous diseases are carried out. However, the impact of bortezomib on synovial sarcoma has not been investigated yet. Therefore, this study aims to provide information about:

- **Characterization of the synovial sarcoma** cell line and **confirmation of the mesenchymal origin.**

- **Cell viability and growth behavior** in presence and absence of bortezomib.

- **Cell cycle distribution** under the influence of bortezomib.

- Determination of the **activity of certain genes** in presence of bortezomib.

2 Methods

2.1 Cell lines

The SW-982 synovial sarcoma cell line shows an adherent growth pattern, a mixed morphology and was retrieved from a 25 years old Caucasian woman [40].

To show and compare the influence of bortezomib on cells which are not malign degenerated, cells from the normal synovial tissue were used. These cells were retrieved from patients of the LKH-Graz and referred to as fibroblast-like synoviocytes (FLS) in the following.

2.1.1 Cell Culture Conditions

The SW-982 synovial sarcoma cell line and FLS were cultured in Dulbecco´s modified Eagle medium DMEM/F12 (Gibco®, Invitrogen, Darmstadt, Germany). The medium was supplemented with 10% foetal bovine serum (FBS) (Gibco®, life technologies™), 0.11% amphotericin B (PAA Laboratory, Pasching, Austria), 1.1% l-glutamine (Gibco®, life technologies™) and 1,1% penicillin/streptomycin (Gibco®, life technologies™).

The cell culture medium (CCM) was changed every three to four days and cells were passaged after reaching a microscopy judged confluence around 80%. The cell detachment was done by Accutase (PAA Laboratory, Pasching, Austria). Cells were kept and cultured in a humidified atmosphere of 37°C with 5% CO_2 and regularly checked on contaminations.

2.1.2 Short tandem repeat (STR) analysis

Short tandem repeats (STRs), sometimes referred to as simple sequence repeats or microsatellites, are usually consisting of a unit between two and seven base pairs. These units are repeated up to several dozen times in a row [41]. STRs are subjected to a high mutation rate, which explains the enormous pluralism in the human population. The polymorphic nature of the analyzed STR loci, allows the discrimination between two or more DNA profiles [41, 42].

STR analysis is highly specific and currently valid as state-of-the-art technique for forensic DNA profiling as well as genetic linkage analysis [42]. From the thousands of STR markers in the human genome, only a small set of loci is used in testing the human identity [43].

2.1.2.1 Execution

To ensure that the maximum of $5x10^6$ cells is not exceeded, they were counted after detachment. Subsequently, the cells were centrifuged for 4 minutes at 1000 rpm. The supernatant was completely removed and the resulting pellet was resuspended in phosphate-buffered saline (PBS) 1x (Gibco®, life technologies™, Carlsbad, U.S.A.) to a final total volume of 200 µl. The following DNA isolation was performed with the silica-membrane-based QIAamp DNA Mini Kit (Qiagen, Hilden, Germany) according to the manufacture´s handbook [63]. The verification of SW-982 cell line was carried out externally with usage of a Powerplex16 System Kit (Promega, Mannheim, Germany).

2.1.3 Vimentin-DAPI Immunofluorescence

To verify the mesenchymal origin of the SW-982 cell line and the FLS, a vimentin-DAPI immunofluorescence analysis was performed at both. Vimentin is a part of the cytoskeleton of vertebrate cells or rather it is an intermediate filament which is involved in cell motility, resistance against mechanical stress and maintenance of the cellular integrity. Intermediate filaments are divided in V classes, comprising XI groups, whereby vimentin belongs to class III [44, 45]. Vimentin is ubiquitously expressed in mesenchymally-derived cells and therefore it can be used as a marker to prove the mesenchymal origin of cells [46].

At first, cells were labeled with a monoclonal mouse- anti-vimentin antibody (Dako, Santa Clara, U.S.A.) and afterwards with a goat anti-mouse antibody (Jackson ImmunoResearch, West Grove, U.S.A.). The latter antibody is cyanin-2 (cy-2) conjugated, which serves as fluorescence dye and links to the first antibody. Furthermore, the cells were counterstained with 4´, 6-diamidino-2-phenylindole (DAPI) which binds to DNA and provides a higher validity in relation to imaging and analysis. The stained cell complex was analyzed and judged with a fluorescence microscope.

2.1.3.1 Execution

As a first step, the SW-982 and FLS were plated into chamber slides with approximately 2500 cells/well. After incubation, the cells were washed with phosphate-buffered saline (PBS) 1x (Gibco®, life technologies™, Carlsbad, U.S.A.) and then dried for about one hour at room temperature (rt). The dried cells were stored overnight at -20 °C. In a next step, the cells were fixed with paraformaldehyde [4%] (pFA) and afterwards washed with PBS 1x (Gibco®) for the second time.

To reduce unspecific protein bindings and improve the imaging quality, the cells were treated with UltraVision Protein Block (Thermo Fisher Scientific). With an antibody diluent, consisting of 0,3% Triton™ X-100 (Sigma Aldrich) and 1% bovine serum albumin (BSA) in PBS 1x (Gibco®), the vimentin antibody (156 mg/L) (Dako) as well as the goat anti-mouse antibody (1,5 mg/ml) (Jackson ImmunoResearch) were prepared in a 1:100 solution. After five minutes of incubation the UltraVision Protein Block (Thermo Fisher Scientific) was knocked off carefully and 200µl of the diluted first antibody (Dako) was added to each well. After 30 minutes of incubation, the cells were rinsed with PBS 1x (Gibco®) again and the diluent, containing the cy-2 conjugated goat anti-mouse antibody (Jackson ImmunoResearch), was added (200 µl per well). After the cells were incubated for a further 30 minutes (protected from light at rt), they were washed with PBS 1x (Gibco®) again and subsequently counterstained with a Vectashield Mounting Medium containing DAPI (Vector Laboratories, Burlingame, U.S.A.).

In order to obtain significant results, controls were performed (Tab. 1).

Negative control	**Antibody-diluent**
Negative control	**Antibody-diluent + mouse immunoglobulin G (IgG)**
Negative control cells	**MCF7 cells**
Positive control cells	**HeLa cells**

Table 1. Vimentin-DAPI immunofluorescence controls.
The MCF-7 cell line was derived from human cervical cancer cells and the HeLa cell line from human breast cancer cells.

The cells were stored light-excluded and visualized with a Confocal LSM 510 META Fluorescence Microscope (Zeiss, Vienna, Austria) which worked with ZEN 2009 software (Zeiss).

2.2 Cell viability assay

To determine the number of viable cells under the influence of certain bortezomib (Selleckchem, Houston, TX) concentrations and to calculate the half maximal inhibitory concentration (IC_{50}), a CellTiter 96® AQ_{ueous} One Solution Cell Proliferation Assay (Promega) was performed. CellTiter 96 (Promega) contains a tetrazolium compound (3-(4,5-dimethylthiazol-2-yl)-5-(3-carboxymethoxyphenyl)-2-(4-sulfophenyl)-2H tetrazolium, inner salt; MTS) and an electron coupling reagent called phenazine ethosulfate (PES).

Metabolically active cells are bioreducing the MTS tetrazolium compound (Owen's reagent) in a colored formazan product (Figure 10). This conversion is most probably accomplished by NADPH or NADH [47]. The absorbance of the colored formazan product is directly proportional to the amount of living cells in culture and was measured with a 96-well plate reader at a wavelength of 490 nm.

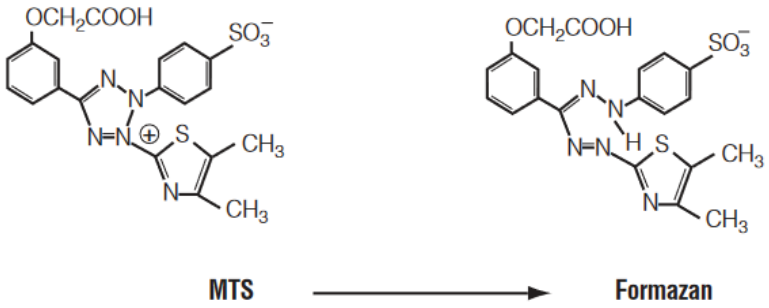

Figure 10. Structures of MTS tetrazolium and its formazan product.
Source adapted from: [48]

2.2.1 Execution

The cells were counted with a Neubauer chamber and subcultured in the needed cell-concentrations (cell type and experiment dependent cell numbers are shown in Tab. 2). In a next step they were plated with their above described culture medium into a 96-well plate. Overall, four independent experiments, each in quadruplicates, were performed.

	Experiment 1	Experiment 2	Experiment 3	Experiment 4
SW-982	3000 cells/well	3000 cells/well	3000 cells/well	3000 cells/well
FLS	3000 cells/well	3000 cells/well	4000 cells/well	5000 cells/well

Tab. 2. The used cells/well for each experiment (cell viability assay).
The cell numbers had to be adjusted due to the different growth behaviour.

Following 24 hours of incubation, the cells were treated with different concentrations of bortezomib (0,5 nM, 1nM, 2,5 nM, 5 nM, 10 nM, 25 nM, 50 nM , 100 nM, 250 nM). Also, a control plate with untreated cells was measured.

Plates were measured after 24, 48 and 72 hours of treatment with bortezomib. Two hours before measurement, 20 µl of CellTiter 96® reagent was added to each well and, subsequently, the cells were incubated under light protection at 37°C and 5% CO_2. To analyze the absorbance values of the formazan product, a Spektrostar NANO microplate reader (BMG LabTech, Ortenberg, GER) was used.

2.3 xCelligence real-time cell analysis

The xCELLigence system (ACEA Biosciences Inc., San Diego, U.S.A) allows to monitor cell proliferation and phenotypic changes in real time. It works by measuring the electrical impedance across micro-electrodes (gold biosensors) which are embedded at the base of 16-well E-plates® (Roche Diagnostics, Switzerland). Only adherent cells are able to interact with the integrated micro-electrodes and generate a quantifiable impedance which correlates with the biological cell status (Figure 11). The biological status of cells, comprising cell viability, morphology and cell number, is displayed as dimensionless value called cell index (CI).

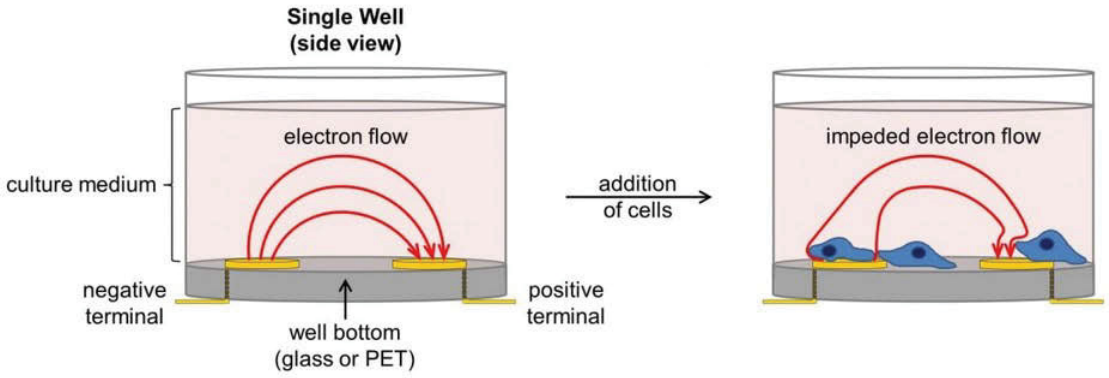

Figure 11. The cellular impedance apparatus (xCELLigence Real-time cell analysis).
If adherent cells proliferate on the gold biosensors, the current electric flow is hindered and provides a sensitive readout of cell size, morphology, cell number and attachment quality. Source adapted from: [49].

2.3.1 Execution

At first, SW-982 and FLS were counted and subcultured in needed concentrations. Before the cells were seeded into 16-well E-plates® (Roche Diagnostics), a background test with culture medium (without cells) was performed. The cells were added into 16-well E-plates® (Roche Diagnostics) with 100µl of their culture medium and afterwards incubated for approximately 24 hours. The numbers of seeded cells are shown in Figure 12.

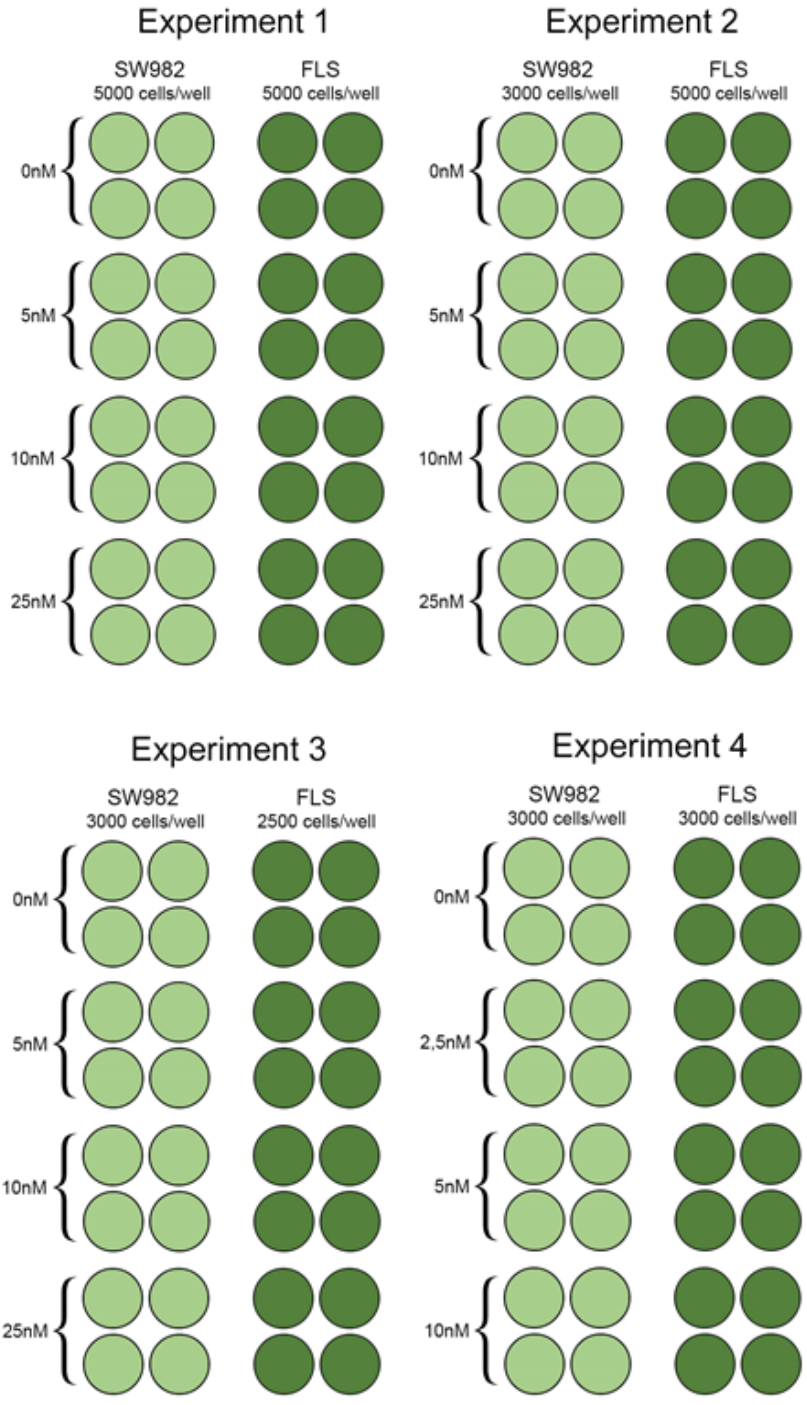

Figure 12. Schematic figure of 16-well E-plates® (Roche Diagnostics).
Seeding setup and bortezomib concentrations for each experiment. Due to the different cell morphology and growth behavior, cell numbers had to be adjusted. Source: PG

As a next step, the CCM was removed and discarded in order to add various concentrations of bortezomib dissolved in 100µl culture medium according to Figure 12. Also a control plate with untreated cells was performed.

Measurements were performed every 20 minutes for a period of 120 hours. The xCELLigence device System worked with RTCA software (Version 1.2, ACEA).

2.4 Quantitative real- time Polymerase Chain Reaction

The RT-qPCR is a method of amplification for nucleic acids based on the principle of conventional polymerase chain reaction (PCR). The RT-qPCR additionally allows the quantification of the obtained DNA.

Principle of PCR:

This revolutionary method is based on the property of DNA polymerase to generate a new, complementary DNA strand to an offered template strand. A new nucleotide can only be added onto a pre-existing hydroxy group at the target sequence. Primers have the ability to provide such a suitable hydroxy function with their 3'-OH end. Furthermore, primers are specific for a DNA sequence and therefore they can be used to amplify a certain region of a template DNA sequence up to several million times [50]. The major processes of PCR are depicted and explained in Figure 13.

The main components for PCR comprise sample DNA or, like in this case, complementary DNA (cDNA) which contains the sequence of interest. Complementary DNA is synthesized from a single stranded RNA template. This conversion is catalyzed by an enzyme called reverse transcriptase. Further, DNA polymerase as well as heat resistant primers, which are complementary to the target DNA/cDNA sequence, are required. Also, deoxyribonucleotides, the components DNA is composed of, are necessary for the polymerase chain reaction [51, 52].

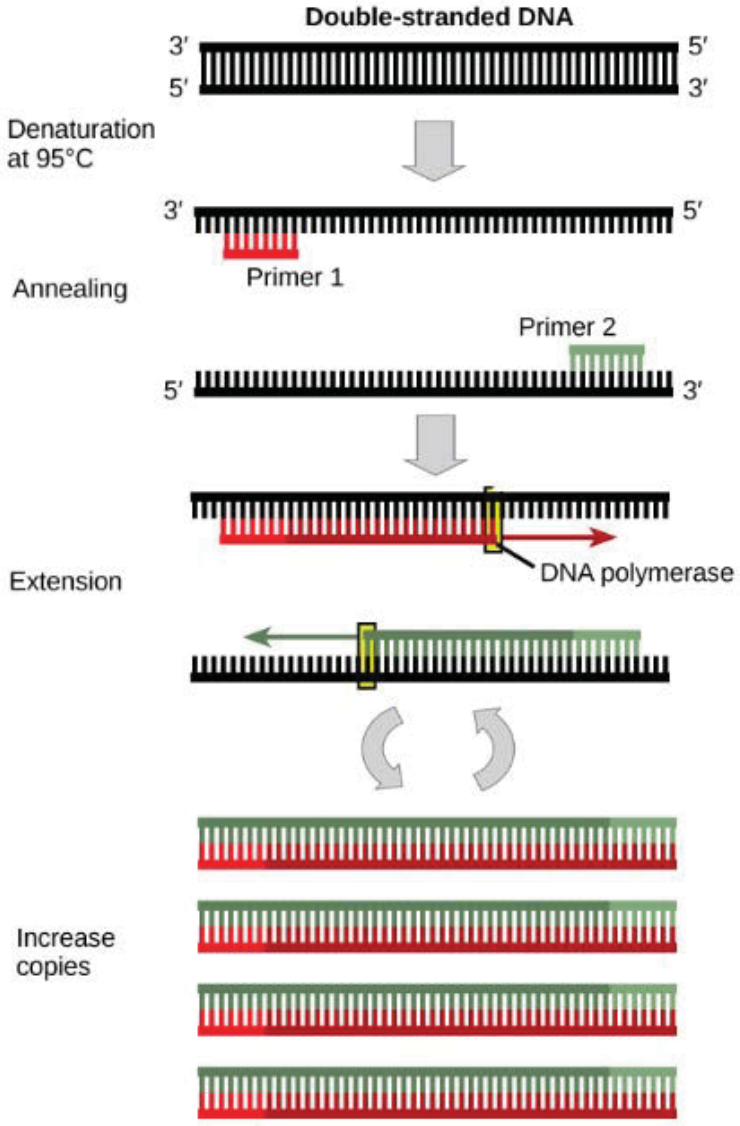

Figure 13. PCR processes depicted in a simplified approach.
The first step is the separation of the dsDNA through raising the temperature to 95°C. Subsequently, temperature is lowered to facilitate annealing of primers to the single stranded DNA (ssDNA) templates. For the primer extension, a DNA polymerase depending raise of temperature is required. At this stage, the DNA polymerase adds free deoxyribonucleotides from the reaction mixture and generates a new DNA strand which is complementary to the template strand. To create many copies of the sequences of interest, these steps are repeated cyclically [54]. Source adapted from: [53]

Essential steps preceding RT-qPCR

At first, the RNA from treated as well as untreated cells was isolated and purified by using the RNeasy Mini Kit (Qiagen, Hilden, Germany). Afterwards, the purified RNA was subjected to quantity- and quality assessment performed by NanoDrop 1000 spectrometer (Thermo Fisher Scientific, Waltham, U.S.A.) and a BioAnalyzer (Agilent 2100, Agilent Technologies, Santa Clara, U.S.A.), respectively. For the next step, DNA-free RNA is essential. Therefore, potentially present genomic DNA was removed with the Thermo Scientific™ DNase I, RNase-free kit (Thermo Fisher Scientific).

Subsequently, the RNA was converted into cDNA by using reverse transcriptase from BioRad (iScript™). The obtained cDNA was used to perform the RT-qPCR.

The mentioned steps above are described in more detail in chapter 2.4.1–2.4.5.

2.4.1 RNA Isolation

The utilized RNeasy Mini Kit (Qiagen, Hilden, Germany) provides a RNA purification by using RNeasy spin columns (Qiagen, Hilden, Germany) with a silica-membrane. The procedure of RNA isolation consists of several steps starting with cell-lysis and homogenizing in presence of a denaturing guanidine-thiocyanate–containing buffer. This buffer promptly inactivates RNases to guarantee purification of RNA. To create conditions under which a selective binding of RNA to the silica-membrane is feasible, ethanol must be added to the lysate. A specialized high-salt buffer system enables RNA with a length over 200 bases, to attach to the silica-membrane of the RNeasy spin columns. After a few washing steps, performed by centrifugation, isolated RNA was eluted into 30 µl of RNase-free water. The steps are illustrated in the following Figure 14.

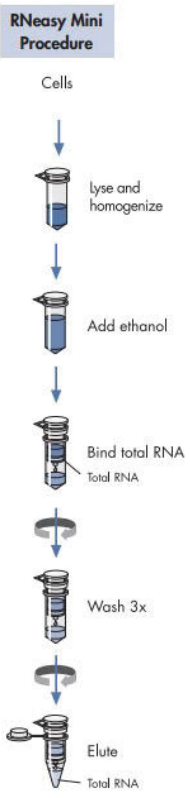

Figure 14. The steps of the RNase Mini procedure.
Source adapted from: [56]

2.4.1.1 Execution

At first, $2x10^6$ SW-982 cells were seeded into petri-dishes and replenished to 7ml with CCM. After approximately 24 hours of incubation, the cells where treated with 5nM and 10nM bortezomib. In addition, also a non-treated control group was performed. After the treatment, the cells were incubated for further 48 hours. Subsequently, the CCM was carefully removed by suction and the cells were washed with PBS 1x (Gibco®). To lyse the cells, 350µl RLT Buffer- (Qiagen, Hilden, Germany) β-mercaptoethanol- (β-ME) mixture (100:1 ratio) was pipetted into each petri-dish. Next, the cells were pooled off with a cell scraper to transfer the lysate into RNeasy spin columns (Qiagen) prefilled with 350µl ethanol [70%]. Afterwards, the cells were centrifuged at 10.000 rpm for 30 seconds. After the centrifugation, the flow-through was discarded and 700 µl RW1 Buffer (Qiagen, Hilden, Germany) was added. The RNeasy spin columns (Qiagen) were placed into the centrifuge and rotated at 10.000 rpm for 30 seconds. After the flow-through was discarded again, the following steps were performed:

- 500µl RPE Buffer (Qiagen) was added
- Centrifuged at 10.000 rpm for 30 seconds (flow-through was discarded)
- 500µl RPE Buffer (Qiagen) was added
- Centrifuged at 10.000 rpm for 2 minutes (flow-through was discarded)
- Collection tubes were renewed
- Centrifuged at 10.000 rpm for 1 minute (to dry the membrane of the RNeasy spin columns (Qiagen))
- 30µl of RNase-free water (Qiagen) was added
- Centrifuged at 10.000 rpm for 1 minute to obtain the isolated, diluted RNA

To bridge the time period between RNA isolation and the next usage, the purified RNA was immediately frozen at -80°C.

2.4.2 Quantity assessment of purified RNA

Before a RNA quality assessment was performed, the RNA concentration of each sample was measured by utilizing a NanoDrop 1000 spectrometer from Thermo Fisher Scientific (Waltham, U.S.A.).

The NanoDrop 1000 is a full spectrum (220nm-750nm) spectrophotometer whereby the absorption maximum of RNA amounts 260 nm. Contaminations, such as phenol or proteins, have its absorption maximum at about 280 nm. Therefore, absorption ratios of 260 nm and 280 nm were used to assess the RNA quantity and purity [57].

2.4.2.1 Execution

To "blank" the spectrophotometer (Thermo Fisher Scientific), RNase-free water was used. Subsequently, the samples (2 µl of each) were pipetted on the sample pedestal and measured. The sample absorbance was calculated by involving the blank absorbance (-log(sampleintensity/blankintensity)). The correlation of absorbance and concentration was computed with the Beer-Lambert equation [57].

2.4.3 Quality assessment of purified RNA

The quality assessment of purified total RNA was carried out with an Agilent 2100 BioAnalyzer from Agilent Technologies (Santa Clara, U.S.A.). The BioAnalyzer (Agilent Technologies) uses a "lab on a chip" technique to accomplish capillary electrophoresis. For determination of RNA concentration and RNA integrity a fluorescent dye, that intercalates into RNA, was used. The chip comprises gel- and sample wells as well as an external standard well. These wells are interconnected with micro-channels made of glass [58].

The BioAnalyzer (Agilent Technologies) integrates the chip of the filled and prepared wells in an electrical circle. The voltage gradient electrophoretically drives the charged RNA biomolecules. Due to the mass/charge ratio and the sieving polymer matrix, the biomolecules are divided by size. The RNA linked dye molecules are detected by laser-induced fluorescence and become displayed as bands (gel-like images) and peaks (electropherograms). The unknown samples are compared to the ladder fragments to assess the concentration of the samples.

To improve the reproducibility, a dimensionless value called RNA Integrity Number (RIN) was invented. RIN is based on a software algorithm and ranging from 1-10 whereby 1 correlates to the most degraded and 10 to the most intact RNA [59].

2.4.3.1 Execution

The chips were prepared and micro-channels were filled with a sieving polymer as well as the fluorescence dye. 1 µl of each RNA sample was used to determine the purity and concentration. All steps were performed according to the Agilent 2100 Bioanalyzer 2100 Expert User's Guide [58].

2.4.4 Removal of genomic DNA

The preparation of DNA-free RNA is essential for the proper conduct of RT-qPCR. The used endonuclease, Thermo Scientific™ DNase I, RNase-free (Thermo Fisher Scientific) digests ssDNA and dsDNA by hydrolysing certain phosphodiester bonds. DNase I (Thermo Fisher Scientific) is activated by Mn^{2+} or Mg^{2+} (Figure 15) and its activity is dependent on Ca^{2+} ions [60].

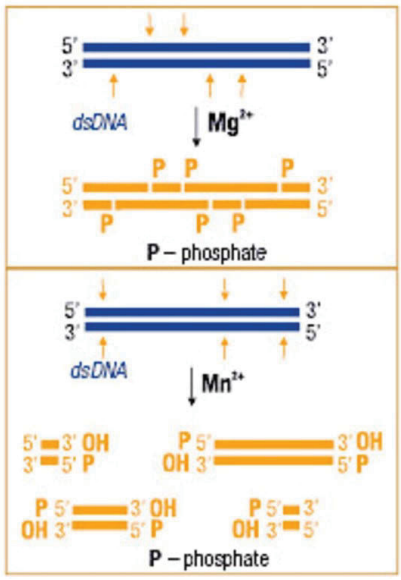

Figure 15. Activity of DNase I (Thermo Fisher Scientific) in the presence of Mg2+ and Mn2+.
Mg^{2+}: The enzyme cleaves both strands of dsDNA independently in a random way. Mn^{2+}: The enzyme cleaves each of the dsDNA strands at similar positions. The resulting DNA fragments have blunt ends or one-two nucleotide overhangs. Source adapted from: [60]

2.4.4.1 Execution

At first, 1 µL of 10X Reaction Buffer, 1 µL of DNase I, RNase and 1 µg of purified RNA, according to the Agilent 2100 BioAnalyzer results, was added to a RNase-free tube. The used 10X Reaction Buffer is composed of 100 mM Tris-HCl (pH 7.5 at 25°C), 1 mM $CaCl_2$ and 25 mM $MgCl_2$ [61].

To obtain the required total volume of 10 µL, the mixture was filled up with diethylpyrocarbonate (DEPC) -treated water. To initiate the digesting process, the mixture was incubated for 30 minutes at 37°C. Subsequently, 1 µL ethylenediaminetetraacetic acid (EDTA) (50 mM) was added to inactivate the RNase. After a further incubation at 65°C for 10 minutes, in presence of EDTA, the RNA sample was prepared for complementary DNA synthesis.

2.4.5 Complementary DNA Synthesis

For the conversion of RNA to cDNA the iSCript™ cDNA Synthesis Kit from BioRad Laboratories (Hercules, U.S.A.) was utilized. The included iScript Reverse Transcriptase is obtained from a modified Moloney murine leukemia virus (MMLV) and is optimized for cDNA synthesis. Furthermore, the Synthesis Kit comprises the 5x iScript Reaction Mix which contains the required primers. This certain blend of random hexamer and oligo primers works great with a wide range of targets [62].

2.4.5.1 Execution

11 µl of the RNA template, 4 µl of 5x iScript™ reaction mix and 1 µl of iScript™ reverse transcriptase were added to 4 µl nuclease-free water. The complete reaction composite was incubated in a thermal cycler according the protocol depicted in Table 3.

Priming	5 minutes at 25ºC
Reverse transcription	30 minutes at 42ºC
Inactivation of reverse transcription	5 minutes at 85ºC
Hold at	4ºC

Table 3. Thermal cycler protocol.

2.4.6 Real Time – quantitative Polymerase Chain Reaction

The quantification of the real-time PCR can be realized in several ways. In this study, a SsoAdavanced™ Universal SYBR® Green Supermix (BioRad) based measurement, which was recorded in real time during a PCR cycle, was performed.

Fluorescence dyes employed for this purpose are able to intercalate into double-stranded DNA (Figure 16). Consequently, an increasing amount of product DNA results in an increased fluorescence or rephrased, the measured fluorescence value is proportional to the amount of amplified product [51].

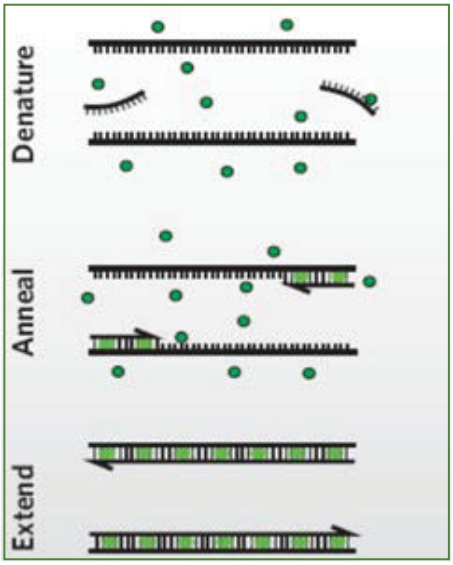

Figure 16. Behavior of SYBR® Green Supermix in different PCR phases.
During annealing phase, the fluorescence dye begins to intercalate into dsDNA. The increasing intercalation in extension phase correlates with the increasing amount of dsDNA. Source adapted from: [55]

In addition to the fluorescence dye (SYBR® Green I dye) the SYBR® Supermix (BioRad) contains $MgCl_2$, dNTPs, stabilizers, enhancers, antibody-mediated polymerase and a compound of passive reference dyes [62].

The following primers were used for amplification:

The QuantiTect® primer assays from Qiagen (Hilden, Germany) for reference genes:

-β-Actin (ACTB)

-Hypox anthine phosphoribosyl-transferase (HPRT-1)

The QuantiTect® primer assays from Qiagen (Hilden, Germany) for target genes:

-Cyclin B1 (CCNB1)

-Cyclin A1 (CCNA1)

-Cyclin-dependent kinase 1 (CDK1)

-Cyclin-dependent kinase 2 (CDK2)

-Cell division cycle 25C (Cdc25c)

2.4.6.1 Execution

At first, the obtained cDNA samples were diluted until a ratio of 12,5 ng cDNA in 1 µl solution was reached. Afterwards, the required reaction setup for RT-qPCR was prepared according to Table 4.

Sso Advanced universal SYBR® Green supermix (2x)	5 µl
Quantitect Primer (10x)	1 µl
Nuclease free water (NFW)	3 µl
Template (cDNA)	1 µl

Table 4. Setup for RT-qPCR.

The components (Table 4) were pipetted into PCR plate wells which were subsequently sealed with a transparent film. Table 5 gives an overview of the wells, the used bortezomib concentrations and the pipetted primers. To ensure a sufficient mixing of the individual components, the plates were vortexed and afterwards centrifuged for 1 minute at 900 rpm.

	1	2	3	4	5	6	7	8	9	10	11	12
A	ACTB SW982 KO	ACTB SW982 KO	ACTB SW982 KO	ACTB SW982 5nM	ACTB SW982 5nM	ACTB SW982 5nM	ACTB SW982 10nM	ACTB SW982 10nM	ACTB SW982 10nM	ACTB NTC	ACTB NTC	ACTB NTC
B	HPRT SW982 KO	HPRT SW982 KO	HPRT SW982 KO	HPRT SW982 5nM	HPRT SW982 5nM	HPRT SW982 5nM	HPRT SW982 10nM	HPRT SW982 10nM	HPRT SW982 10nM	HPRT NTC	HPRT NTC	HPRT NTC
C	CCNA SW982 KO	CCNA SW982 KO	CCNA SW982 KO	CCNA SW982 5nM	CCNA SW982 5nM	CCNA SW982 5nM	CCNA SW982 10nM	CCNA SW982 10nM	CCNA SW982 10nM	CCNA NTC	CCNA NTC	CCNA NTC
D	CCNB SW982 KO	CCNB SW982 KO	CCNB SW982 KO	CCNB SW982 5nM	CCNB SW982 5nM	CCNB SW982 5nM	CCNB SW982 10nM	CCNB SW982 10nM	CCNB SW982 10nM	CCNB NTC	CCNB NTC	CCNB NTC
E	CDK1 SW982 KO	CDK1 SW982 KO	CDK1 SW982 KO	CDK1 SW982 5nM	CDK1 SW982 5nM	CDK1 SW982 5nM	CDK1 SW982 10nM	CDK1 SW982 10nM	CDK1 SW982 10nM	CDK1 NTC	CDK1 NTC	CDK1 NTC
F	CDK2 SW982 KO	CDK2 SW982 KO	CDK2 SW982 KO	CDK2 SW982 5nM	CDK2 SW982 5nM	CDK2 SW982 5nM	CDK2 SW982 10nM	CDK2 SW982 10nM	CDK2 SW982 10nM	CDK2 NTC	CDK2 NTC	CDK2 NTC
G	Cdc25c SW982 KO	Cdc25c SW982 KO	Cdc25c SW982 KO	Cdc25c SW982 5nM	Cdc25c SW982 5nM	Cdc25c SW982 5nM	Cdc25c SW982 10nM	Cdc25c SW982 10nM	Cdc25c SW982 10nM	Cdc25c NTC	Cdc25c NTC	Cdc25c NTC
H	x	x	x	x	x	x	HPRT RT-	HPRT RT-	HPRT RT-	HPRT NK	HPRT NK	HPRT NK

Table 5. Pipetting schedule of the 96 well plate for PCR.

The samples were amplified and quantified with the CFX96 Touch RT-PCR Detection System from BioRad in compliance with the standard temperature steps (Figure 17). In order to confirm the specificity of the amplification a melt curve- and peak analyses according to MIQE guidelines, was performed.

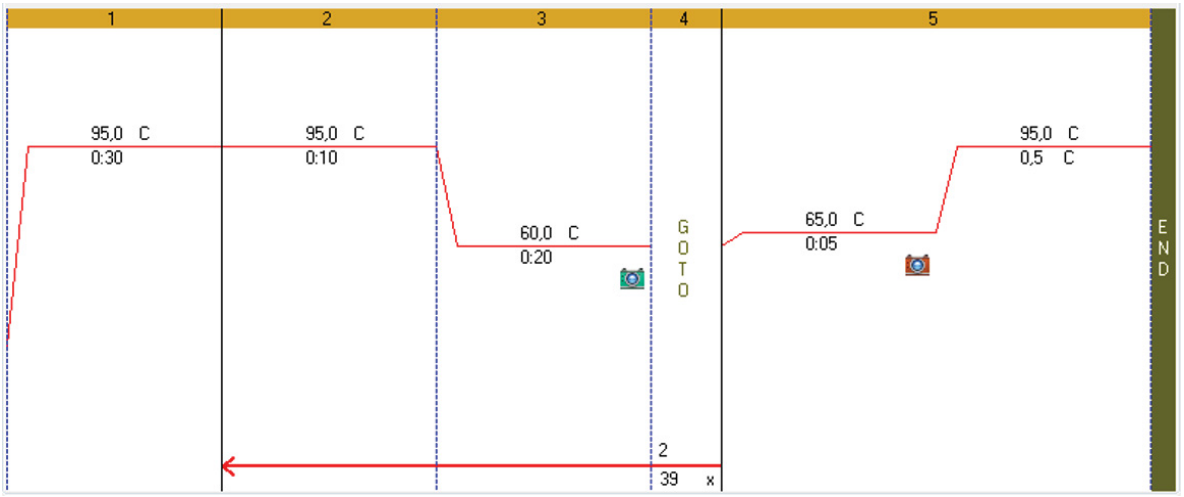

Figure 17. Thermo cycling protocol.
The CFX96 Touch RT-PCR Detection System (BioRad) was set for SYBR Green based measurement. **1.:** cDNA denaturation and polymerase activation (30 sec at 95°C). **2.:** Denaturation (10 sec at 95°C). **3.:** Annealing, extension as well as plate reading (20 sec at 60°C) **4.:** Cycle repeats by starting at point 2. **5.:** Melt curve analysis at 65°C to 95°C and plate reading.

The expression levels were calculated with the ΔΔCt method. To normalize the target gene expression to the reference gene expression, the Ct values of each were subtracted from one another (ΔCt). Subsequently, the ΔCt of target genes were normalized to the untreated control group (ΔΔCt). The obtained values were used to calculate the expression ratio with the $2^{-\Delta\Delta Ct}$ method.

2.5 Flow Cytometry

The used BD™ LSR II cytometer (Biosciences) is based on fluorescence-activated cell scanning and allows the simultaneous measurement of various physical parameters of individual particles in solution. In this case the analysed particles were SW982 cells. The particles (cells) are illuminated with a laser beam. From the resulting scattered light and the fluorescence emission, several parameters can be determined.

Basically, the flow cytometer consists of a liquid system which is responsible for the transport of particles und for their hydrodynamic focussing in a measuring cell. In the

measuring cell the laser beam hits the particles and scatter as well as fluorescence light is subdivided into individual wavelength-packets. Via the optical system, by means of different mirrors and filters, the light is delivered to the different detectors. There the light is switched to electronic signals which are analyzed through a computer software. The schematic structure of a flow cytometer is illustrated in Figure 18.

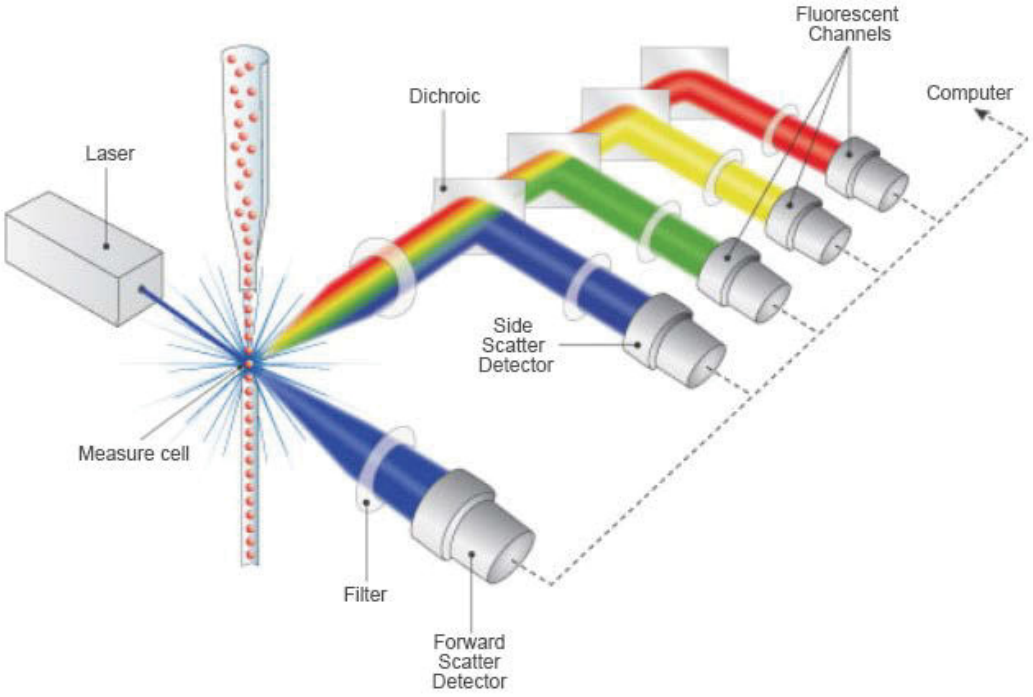

Figure 18. Principle of flow cytometry.
The forward scatter (FSC) detector measures the light coming from the cell in same axis as the laser beam or rather, the light that is deflected at the cell surface. The side scatter detector (SSC) measures the scattered light, which is deflected at an angle of 90° and provides information about the cell granularity. Source adapted from: [64]

As already mentioned in chapter 1.2, the DNA content of cells depends on the cell cycle phase. Therefore, the respective DNA content can be used to determine cell cycle phase. In order to detect the DNA content, utilizing the BD™ LSR II cytometer (Biosciences), the cells were stained with propidium iodide (PI) (Sigma- Aldrich) [65]. Due to cell membrane integrity this fluorescent dye can penetrate the perforated membrane of dead cells but not the intact membrane of living cells. PI binds to dsDNA (by intercalating) and therefore fluorescent detection provides reliable information about the DNA content of the analysed cells [66].

To select the suitable measuring range, the values of the FCS und FFC detector were first plotted on a 2D plot (Figure 19). Subsequently, the selected range was transferred onto a histogram.

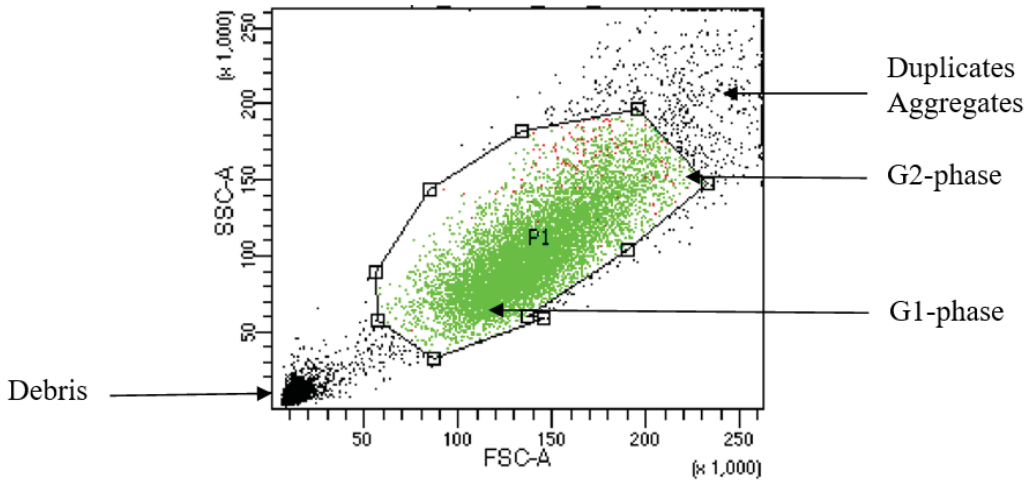

Figure 19. Exemplary depiction of a 2D plot.
The Y-axis corresponds to SSC detector and the X-axis to FSC detector. The green area represents the selected area. A lower fluorescence indicates cells in G1- phase and vice versa a higher fluorescence level indicates cells in G2-phase.

2.5.1.1 Execution

At first $1x10^6$ SW-982 cells were seeded into petri-dishes with 7ml CCM. After approximately 24 hours of incubation, the cells were treated with bortezomib (5nM, 10nM and an untreated control group). Prior to fixation in ethanol [70%], the cells were incubated for a further 24 and 48 hours respectively. By the ethanol fixation and the subsequent storage at -4°C, the cells can be stored up to 2 weeks. The fixation procedure is shown in Table 6.

1. Cells were detached and centrifuged (with supernatant) at 1000 rpm for 4 min. (4°C).
2. The supernatant was discarded and the cell pellet resuspended with 5 ml CCL.
3. Following centrifugation, the cell pellet was resuspended with 0,5 ml PBS 1x (Gibco).
4. The cells were fixated in 5 ml cold ethanol [70%].
5. The cells were stored at -4°.

Table 6. The fixation procedure for flow cytometry.
These steps where performed 24 and 48 hours after the treatment.

All in all three experiments were performed, each in duplicates with an exposure time of 24 hours and 48 hours respectively.

On the day of flow cytometry, a PI-hypotonic lysis buffer was prepared first. The buffer consists of 0,1% sodium citrate tribasic dihydrate (Sigma Aldrich), 0,1% Triton™ X-100 (Sigma Aldrich), 100 µg/ml RNase A (Thermo Fisher Scientific) and 50 µg/ml PI (Sigma-Aldrich). Afterwards, the falcons containing the cells were centrifuged for 4 minutes at 1000 rpm. The resulting cell pellets were resuspended with 200µl PI-hypotonic lysis buffer and transferred to micronics. Prior to flow cytometry, the cells were incubated for approximately 30 minutes at rt in the dark.

The data collected by the BD™ LSR II cytometer (Biosciences) was analyzed using the ModFit LT software Version 4.1.7 (Verity Software House).

3 Results

3.1 Verification of used cells

3.1.1 Short tandem repeat (STR) analysis

In order to confirm the SW-982 cell line, the isolated DNA was compared with reference DNA at the Leibniz-Institut DSMZ (German Collection of Microorganisms and Cell Cultures). Table 7 shows the results or rather the matched sequence repeats in various STR- Loci.

STR-Locus	your cell line	DSMZ
D3S1358	15	
TH01	9.3	9.3
D21S11	28,30	
D18S51	16,18	
Penta E	13,15	
D5S818	11,13	11,13
D13S317	12,13	12,13
D7S820	9,11	9,11
D16S539	11,12	11,12
CSF1PO	11,12	11,12
Penta D	10,13	
Amelogenin	X	X
vWA	19,20	19,20
D8S1179	14	
TPOX	9,11	9,11
FGA	21,24	

Table 7. STR loci comparison of SW-982 and the DSMZ database.

The STRs of the isolated DNA and the reference DNA match in the STR-Loci TH01, D5S818, D13S317, D7S820, D16S539, CSF1PO, Amelogenin, vWA and TPOX. These 9 consensuses furnish clear evidence that the cells used are actually SW-982 cells.

3.1.2 Vimentin-DAPI Immunofluorescence

To confirm the mesenchymal origin of SW-982 cells and the FLS, an immunofluorescence analysis was performed. The green fluorescence, in Figure 20, 22 and 23, is based on high expression of the intermediate filament vimentin stained with a fluorescence dye. Therefore, the mesenchymal origin of these cells shall be deemed to be confirmed. The blue fluorescence correlates to DNA rich regions which were counterstained with DAPI (Figure 20-23). To exclude procedural errors, also a positive and negative control were performed (Figure 20, 21).

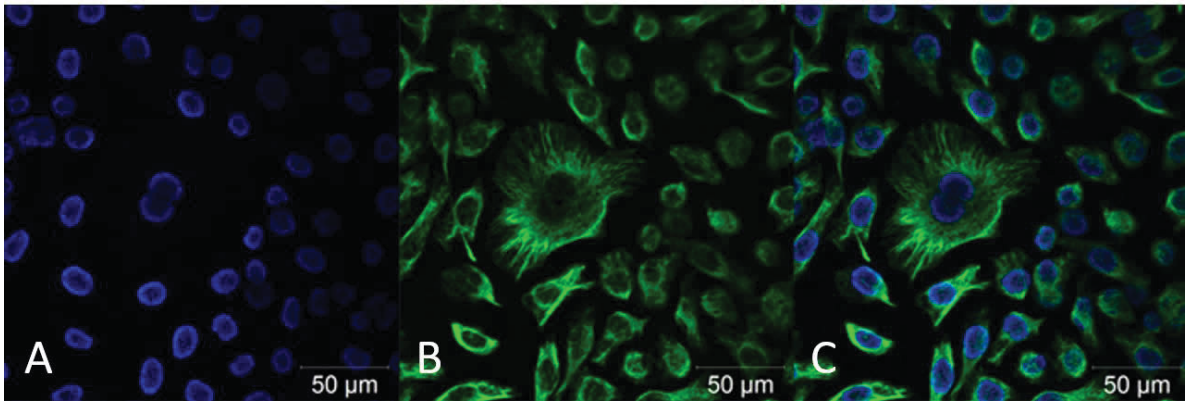

Figure 20. Positive control (HeLa cells).
A: The blue ovoid areas correlates to the DAPI stained DNA (nuclei). **B:** The green regions represents the fluorescence stained vimentin filaments and confirm the mesenchymal origin of the HeLa cells. **C:** The blue DNA (A) and the green vimentin (B) are depicted in this overlay image.

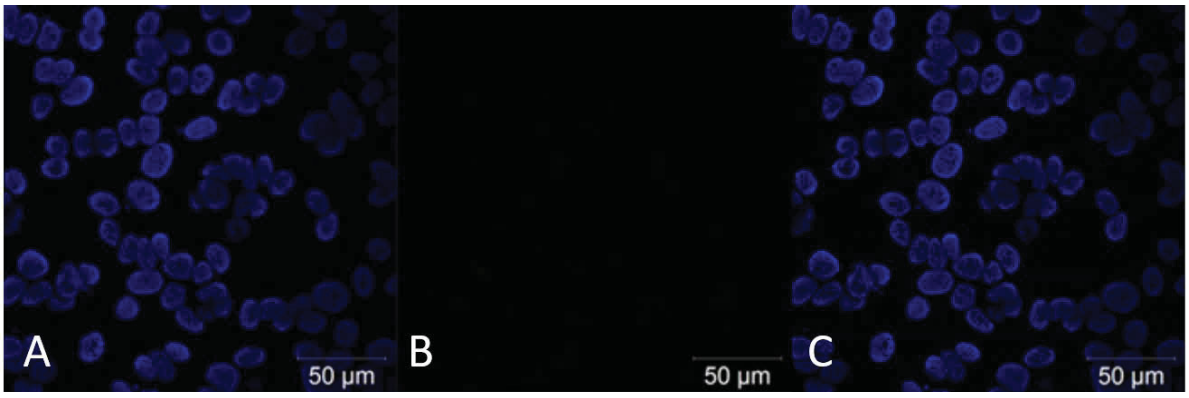

Figure 21. Negative control (MCF7 cells).
A: The blue ovoid areas correlates to the DAPI stained DNA (nuclei). **B:** The absence of green regions indicates a missing vimentin expression. **C**: The overlay image of A and B.

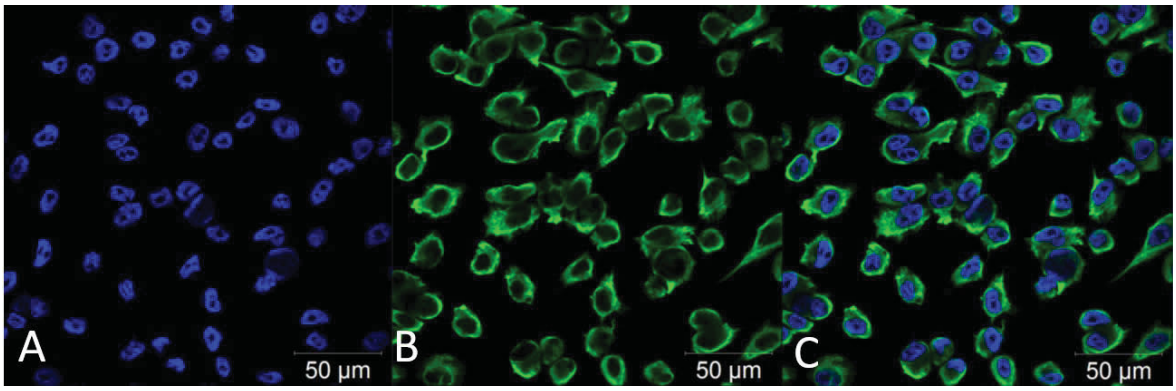

Figure 22. SW-982 cell line.
A: The DAPI stained DNA (nuclei). **B:** The fluorescence stained vimentin filamentsand therefore the confirmation of the mesenchymal origin. **C:** The overlay image of A and B.

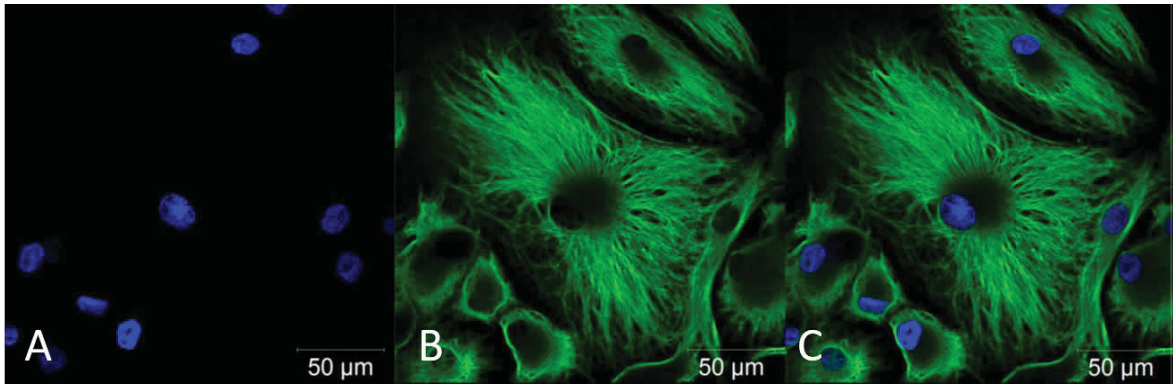

Figure 23. Fibroblast-like synoviocytes (FLS).
A: The DAPI stained DNA (nuclei). **B:** The fluorescence stained vimentin filamentsand therefore the confirmation of the mesenchymal origin. **C:** The overlay image of A and B.

3.2 Cell viability assay (MTS)

The MTS assays (n=4, measured in quadruplicates) were performed 24, 48 and 72 hours after the treatment with bortezomib. The SW-982 cells and the FLS were treated with 0,5 nM, 1nM, 2,5 nM, 5 nM, 10 nM, 25 nM, 50 nM, 100 nM and 250 nM bortezomib. In addition, untreated cells were used as controls.

The MTS assays indicate that the bortezomib treatment has a significant negative, dose-dependent effect on cell viability in both cell lines (Figure 24 A, B; Table 8, 9). Thereby, the cell viability curves show a considerably stronger influence on the SW-982 cells. The significant inhibiting effect on cell viability of SW-982 cells was noticeable even in minor concentrations (Figure 24 A, B).

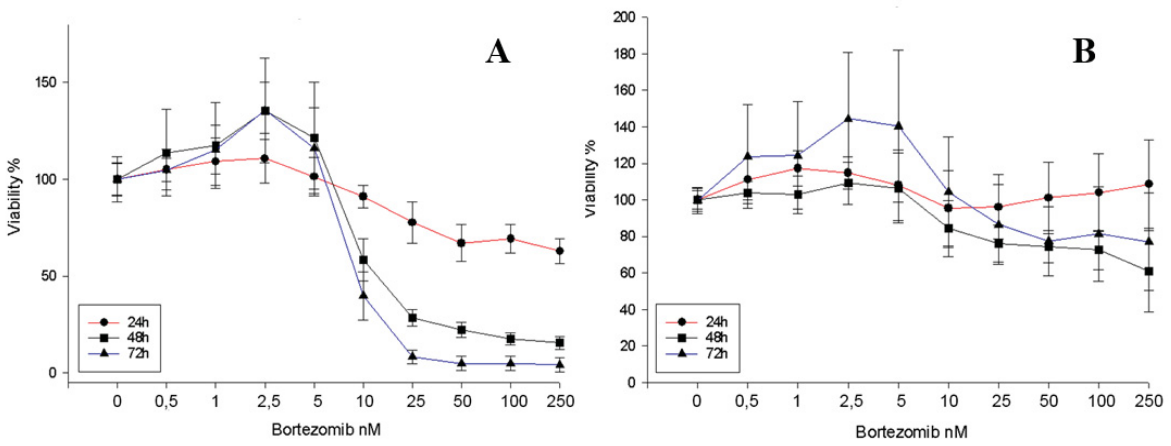

Figure 24. Dose response of SW-982 cells (A) and FLS (B) (±SD).
A: Bortezomib inhibited significantly the growth of SW982 cells in a concentration and exposure time dependent manner. **B:** A considerably impact of bortezomib on viability of FLS was only noticeable in higher concentrations and after a longer exposure time.

Concentrations (nM)	0,0	0,5	1,0	2,5	5,0	10,0	25,0	50,0	100,0	250,0
Exposure time: 24 hours										
Mean ± SD	100 ± 11,8	105,0 ± 10,5	109,1 ± 12,1	110,7 ± 12,8	101,3 ± 10,0	91,1 ± 5,9	77,7 ± 10,6	66,9 ± 9,5	69,3 ± 7,3	62,9 ± 6,4
p-value		0,223	0,039 *	0,029 *	0,741	0,013 *	0,000 ***	0,000 ***	0,000 ***	0,000 ***
Exposure time: 48 hours										
Mean ± SD	100 ± 8,1	113,7 ± 22,3	117,5 ± 22,3	135,4 ± 14,6	121,3 ± 28,8	58,4 ± 11,0	28,6 ± 4,2	22,4 ± 3,9	17,5 ± 3,1	15,6 ± 3,3
p-value		0,033 *	0,008 **	0,000 ***	0,011 *	0,000 ***	0,000 ***	0,000 ***	0,000 ***	0,000 ***
Exposure time: 72 hours										
Mean ± SD	100 ± 8,7	104,8 ± 5,9	115,2 ± 12,6	135,6 ± 27,0	116,0 ± 21,1	39,8 ± 12,4	8,2 ± 3,3	4,9 ± 3,8	4,8 ± 3,7	4,2 ± 3,6
p-value		0,077	0,000 ***	0,000 ***	0,011 *	0,000 ***	0,000 ***	0,000 ***	0,000 ***	0,000 ***

Table 8. Mean ± SD and p-values of proliferation assay of SW-982 cells.

Concentrations (nM)	0,0	0,5	1,0	2,5	5,0	10,0	25,0	50,0	100,0	250,0
Exposure time: 24 hours										
Mean ± SD	100 ± 5,0	111,1 ± 11,1	117,2 ± 9,7	114,7 ± 8,7	108,0 ± 19,5	95,4 ± 20,5	96,2 ± 17,7	101,1 ± 19,5	104,0 ± 21,1	108,6 ± 24,1
p-value		0,001 **	0,000 ***	0,000 ***	0,129	0,395	0,417	0,823	0,470	0,180
Exposure time: 48 hours										
Mean ± SD	100 ± 6,2	103,9 ± 6,1	102,9 ± 10,2	109,3 ± 11,5	106,4 ± 19,1	84,3 ± 15,2	75,9 ± 10,1	74,4 ± 8,9	72,6 ± 10,6	60,9 ± 22,1
p-value		0,082	0,346	0,009 **	0,220	0,001 **	0,000 ***	0,000 ***	0,000 ***	0,000 ***
Exposure time: 72 hours										
Mean ± SD	99,6 ± 7,1	123,7 ± 28,3	124,3 ± 29,5	144,4 ± 36,4	133,6 ± 43,1	104,3 ± 30,2	86,5 ± 21,8	77,4 ± 18,9	70,9 ± 13,6	65,1 ± 8,0
p-value		0,004 **	0,005 **	0,000 ***	0,003 **	0,553	0,034 *	0,000 ***	0,000 ***	0,028 *

Table 9. Mean ± SD and p-values of proliferation assay of FLS.

To clearly emphasize the differences between the impact of bortezomib on FLS and SW-982 cells, Figure 25 compares the effects after 48 and 72 hours at both.

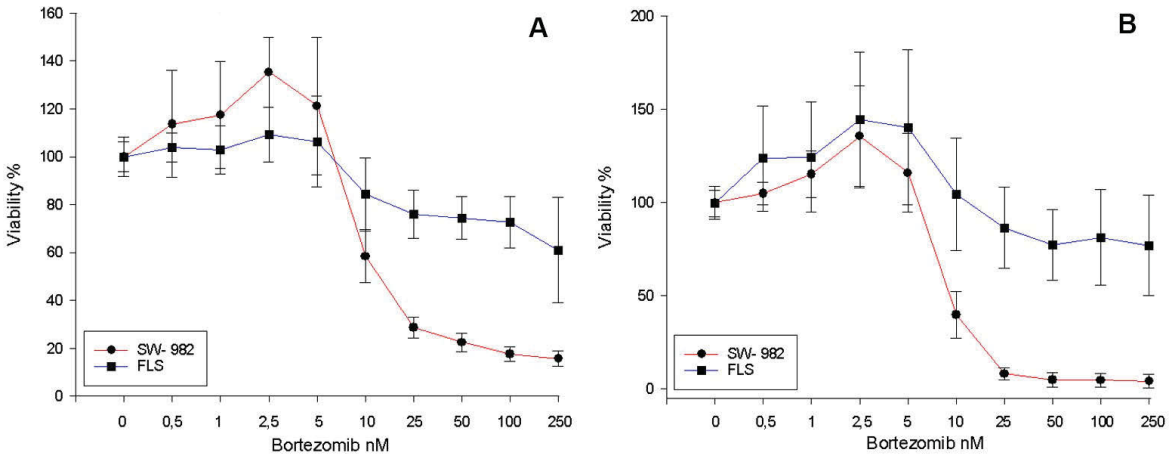

Figure 25. The influence of bortezomib on SW-982 versus FLS.
A: 48 hours after treatment with 25 nM bortezomib the SW-982 cells viability dropped below 30%, however, at the same concentration the cell viability of FLS was still around 75,9% (± 10,1%). **B:** 72 hours after the treatment with 10 nM bortezomib, the viability of SW-982 cells dropped below 40% and by a concentration of 25 nM the viability was even around 8,2% (± 3,3%). Whereas, 72 hours after the treatment with bortezomib in equal concentrations, the viability of FLS was still around 104,3% (± 30,3%) and 86,5% (± 21,8%), respectively.

Based on results of cell viability assays, a half maximal inhibitory concentration (IC_{50}) of 10 nM bortezomib for SW-982 was calculated.

3.3 xCelligence Real-time cell analysis

In order to display the growth behavior of the used cell lines in presence and absence of bortezomib in real time, a xCELLigence System was utilized (n=4, measured in quadruplicates). The used concentration and cell numbers are shown in Figure 12. The cell index was recorded every 20 minutes for 120 hours.

Bortezomib impaired the cell index in both, the SW982 cells and FLS, in a concentration and exposure time dependent manner (Figure 26, 27). Contrary to cell viability assay, a considerably different influence of bortezomib on SW-982 compared to FLS was only noticeable at a concentration of 2,5 nM. At IC_{50} or concentrations above, the SW-982 cell growth curves dropped to 0 within 90 hours after the treatment (Figure 26).

4 days after the treatment with the concentrations 5 nM, 10 nM and 25 nM bortezomib, the effect intensity on FLS was almost equal to SW982 cells. However, the impairment of cell index of FLS was delayed compared to SW982 cells (Figure 27).

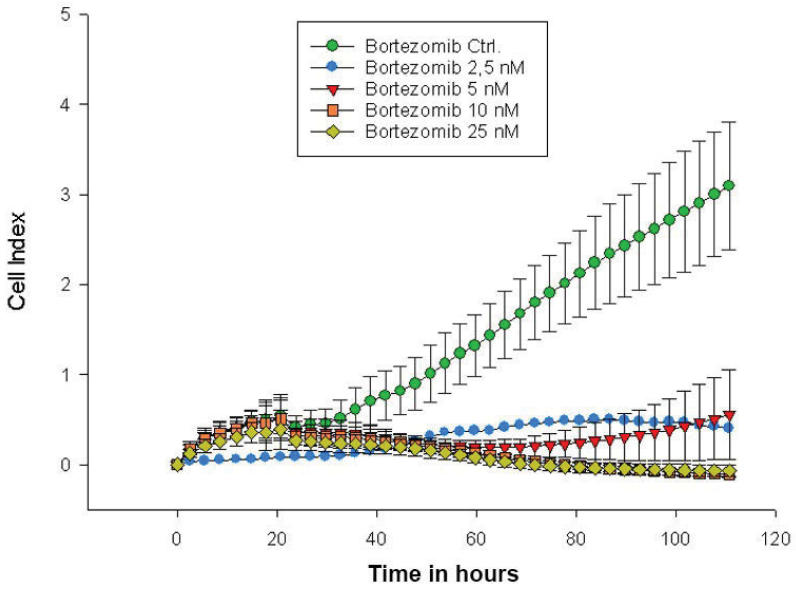

Figure 26. xCelligence analysis of SW-982 cells (±SD).
The treatment was performed at hour 20 (according to time line). A considerably impact of bortezomib on cell index of SW-982 cells was already displayed at a concentration of 2,5 nM.

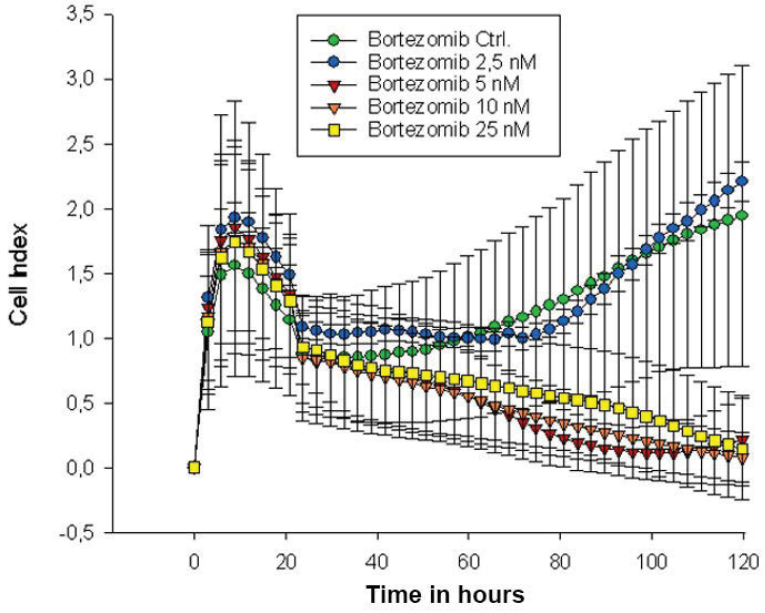

Figure 27. xCelligence analysis of FLS (±SD).
The treatment was performed at about hour 20 (according to time line). A considerably impact of bortezomib on cell index of FLS was displayed at or above a concentration of 5 nM. The cell growth curve of FLS, at a concentration of 2,5 nM, was almost equal to the untreated cells.

Of the four performed experiments, the data of SW-982 cells of the first experiment could not be considered in analysis due to procedural errors. Also the results of the FLS of the second experiment, which were most probably based on pipetting errors, could not be used.

3.4 Gene expression analysis

To obtain information about the gene expression levels of cyclin B1 (CCNB1), cyclin-dependent kinase 1 (CDK1), cyclin-dependent kinase 2 (CDK2) and cell division cycle 25C (Cdc25c) phosphatases a rt-qPCR analysis (n=4, measured in triplicates) was performed. The relative expression of the mentioned genes was normalized on reference genes by the 2-ΔΔCt-method. The expression levels are shown as mean ± SD in Figure 30-33.

3.4.1 Quality assessment of purified RNA

In order to generate information of the quality of the purified RNA the Agilent BioAnalyzer 2100 was utilized. The collected data, depicted in Figure 28 and 29, were run through an intern software algorithm to calculate the RIN values and assess the RNA conditions. Figure 28 shows the calculated RIN values which are ranging from 8,80 to 9,70.

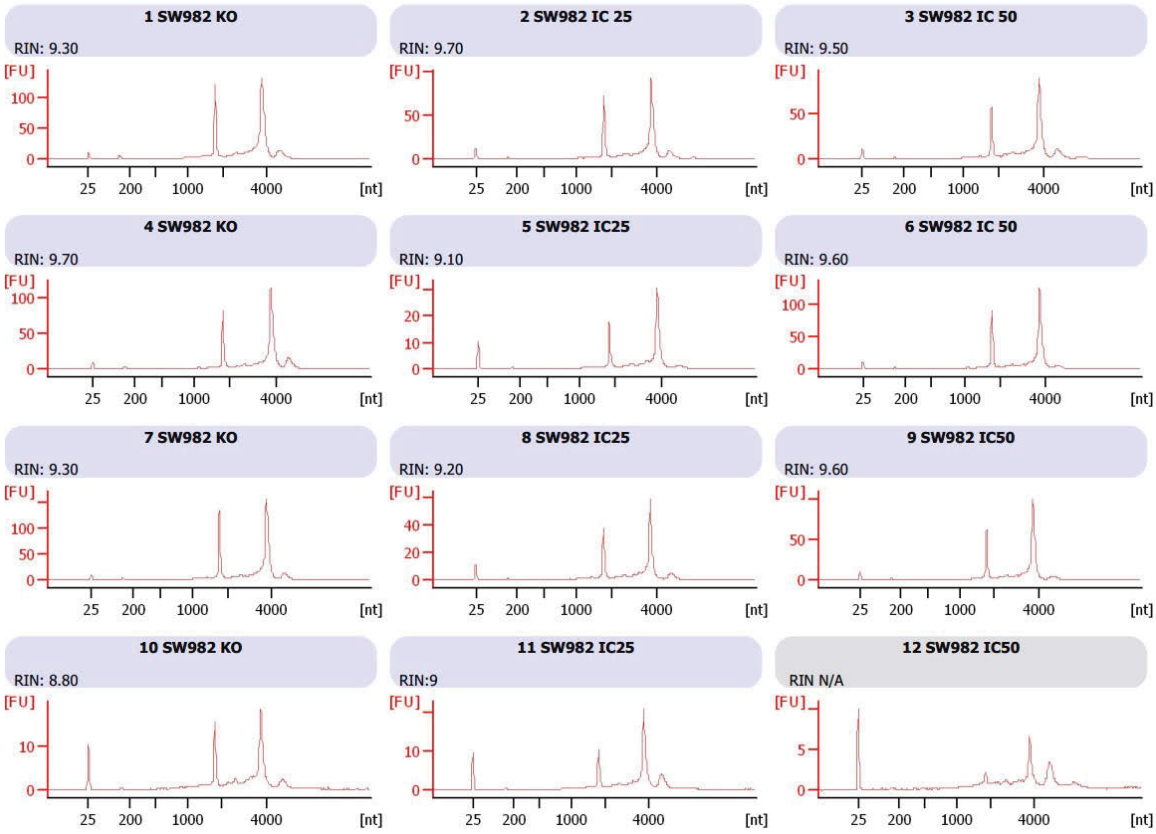

Figure 28. Calculated RIN values of purified DNA samples.
The first, small peaks in front corresponds to the internal marker. The second and third peaks represents the 18S ribosomal and 28S ribosomal peaks, respectively. **1, 2, 3:** Experiment 1. **4, 5, 6:** Experiment 2. **7, 8, 9:** Experiment 3. **10, 11, 12:** Experiment 4. At experiment 4, the RNA, treated with 10 nM (IC_{50}) bortezomib (**12**), could not be analysed.

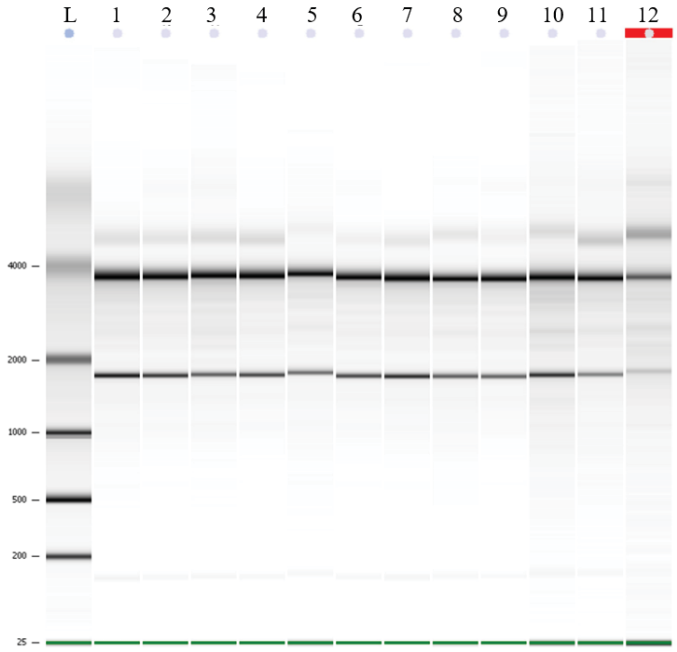

Figure 29. Gel Image of electrophoresis runs.
L: Ladder. **1, 2, 3** (Experiment 1): Control, 5 nM and 10 nM bortezomib. **4, 5, 6** (Experiment 2): Control, 5 nM and 10 nM bortezomib. **7, 8, 9** (Experiment 3): Control, 5 nM and 10 nM bortezomib. **10, 11, 12** (Experiment 4): Control, 5 nM and 10 nM bortezomib. The samples (**1-12**) were compared to the ladder (**L**). The first two bands from top to bottom corresponds to the 28S RNA and 18S RNA strands, respectively. The green bottom bands (25nt) represents the internal markers.

3.4.2 Gene expression levels

CCNB (Cyclin B1):

The SW-982 cells, which were treated with a concentration of 5 nM bortezomib, showed the highest expression level of CCNB. Whereas, the lowest expression tendency was detected at the untreated control group. CCNB expression levels are shown in Figure 30.

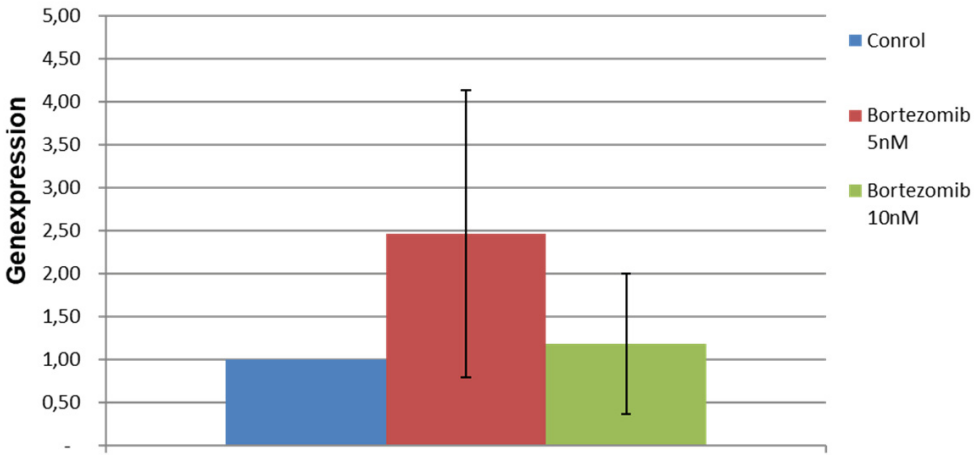

Figure 30. CCNB expression 48 hours after treatment with bortezomib (±SD).

CDK1 (cyclin-dependent kinase 1):

A slight, but not statistical significant increase of CDK1 was measured at a concentration of 5 nM bortezomib. The expression level of the untreated control was almost equal to the cells which were treated with 10 nM bortezomib. Expression levels of CDK1 are shown in Figure 31.

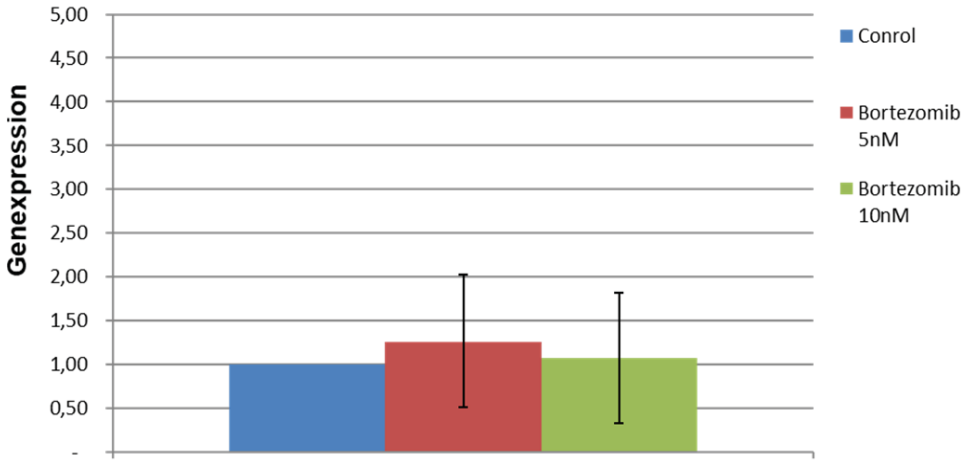

Figure 31. CDK1 expression 48 hours after treatment with bortezomib (±SD).

CDK2 (cyclin-dependent kinase 2):

The treatment with a concentration of 5 nM bortezomib leaded to the highest expression level of CDK2 (p=0,032). To contrast, the SW-982 cells, treated with 10 nM showed the lowest expression (p=0,034). Expression levels of CDK2 are depicted in Figure 32.

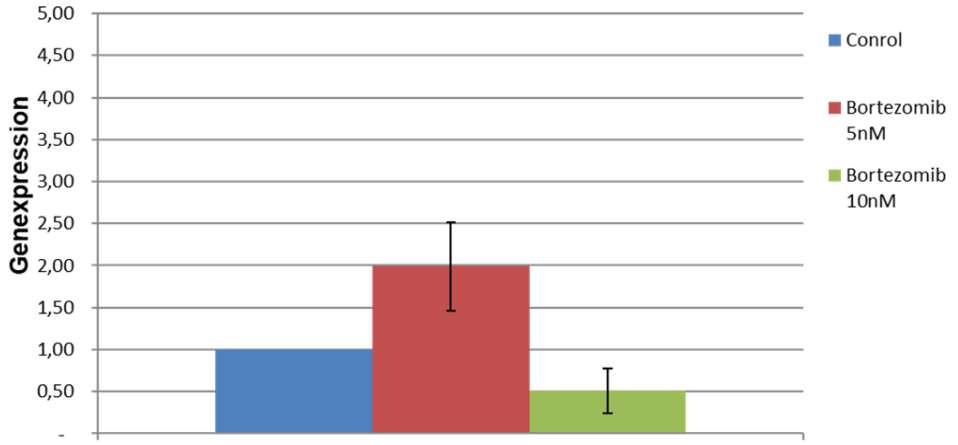

Figure 32. CDK2 expression 48 hours after treatment with bortezomib (±SD).

Cdc25c (cell division cycle 25C):

The highest expression tendency was detected at the concentration of 5 nM bortezomib. At a concentration of 10 nM, the expression level of Cdc25c was almost equal to the untreated SW-982 cells. Figure 33 shows the expression levels of Cdc25c.

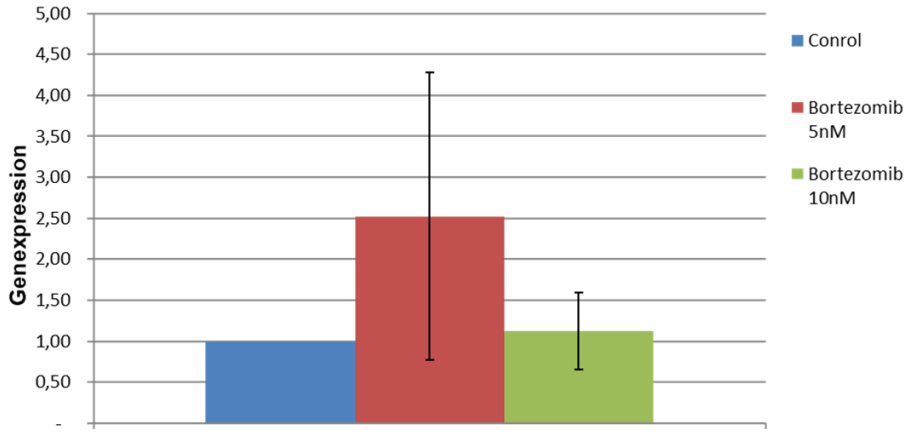

Figure 33. CdC25c expression 48 hours after treatment with bortezomib (±SD).

3.5 Flow Cytometry

To generate information of the DNA content of treated as well as untreated cells and to subsequently determine the cell cycle phase, a flow cytometry, based on fluorescence-activated cell scanning, was performed (n=3).

Bortezomib was applied in a concentration of 5 nM (IC_{25}) and 10 nM (IC_{50}). Prior to flow cytometry, the SW-982 cells were fixated (in ethanol [70%]) 24 and 48 hours after the treatment. The measured data was first displayed in 2D plots. In order to exclude contaminates such as debris and aggregates from final results, the area to be measured was selected manually at the 2D plots. Figure 34 exemplary shows the 2D plots of the first experiment. To facilitate final analysis, the generated data was transferred and displayed in histograms (Figure 35-37).

The data, provided by flow cytometry, indicates that the presence of bortezomib leads to an accumulation of SW-982 in G2-phase and at the same time to a decrease of S-phase as well as G1-phase. As shown in Figures 35-37, the influence on cell cycle distribution was most notably depended on dose.

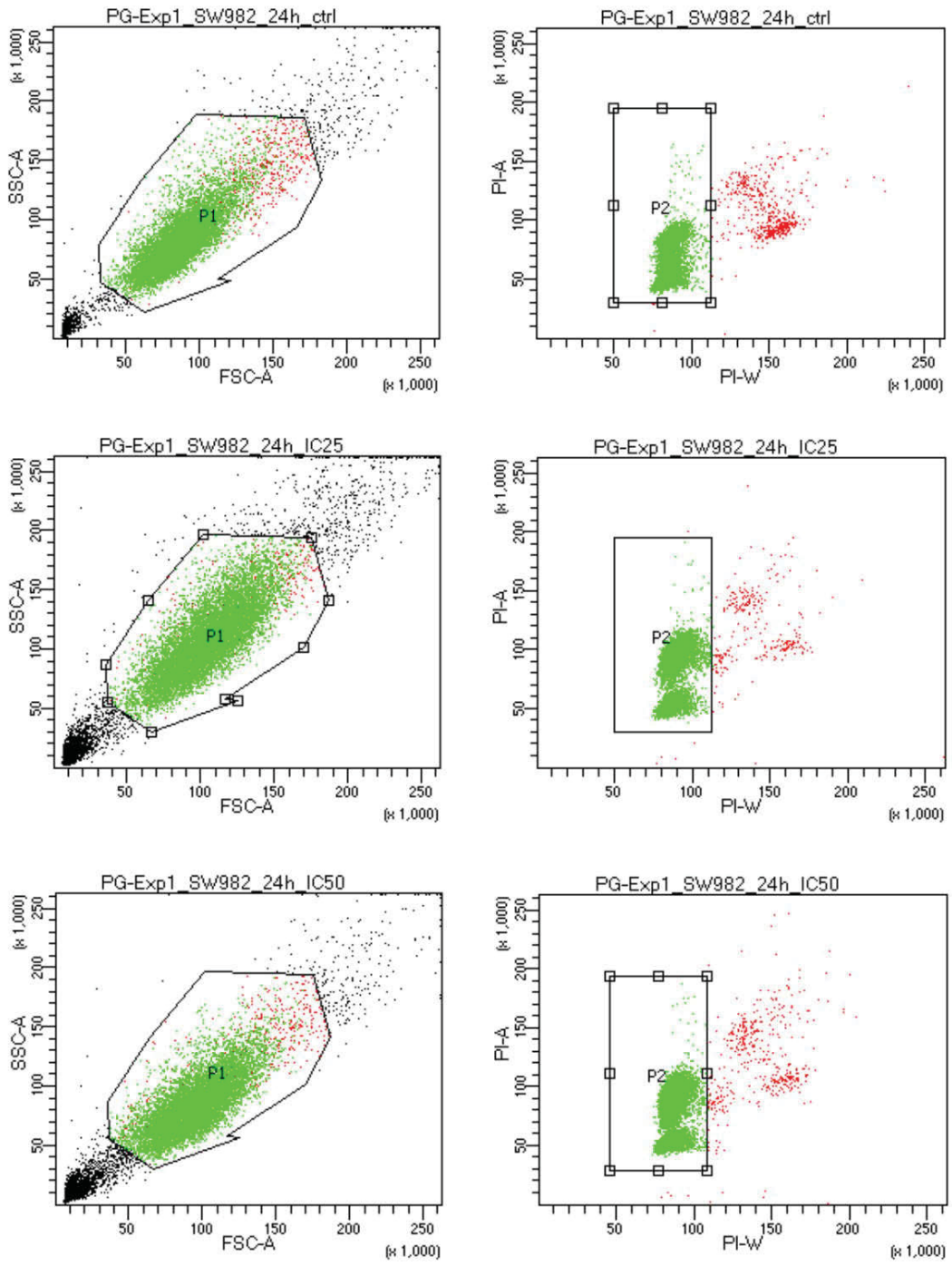

Figure 34. 2D plots of the first experiment (24 hours).
The first 2D plots from left to right corresponds to the untreated control. The middle and the bottom ones corresponds to treated SW982 cells (5 nM, 10 nM). The selected green areas represent the actual DNA contents of the measured cells.

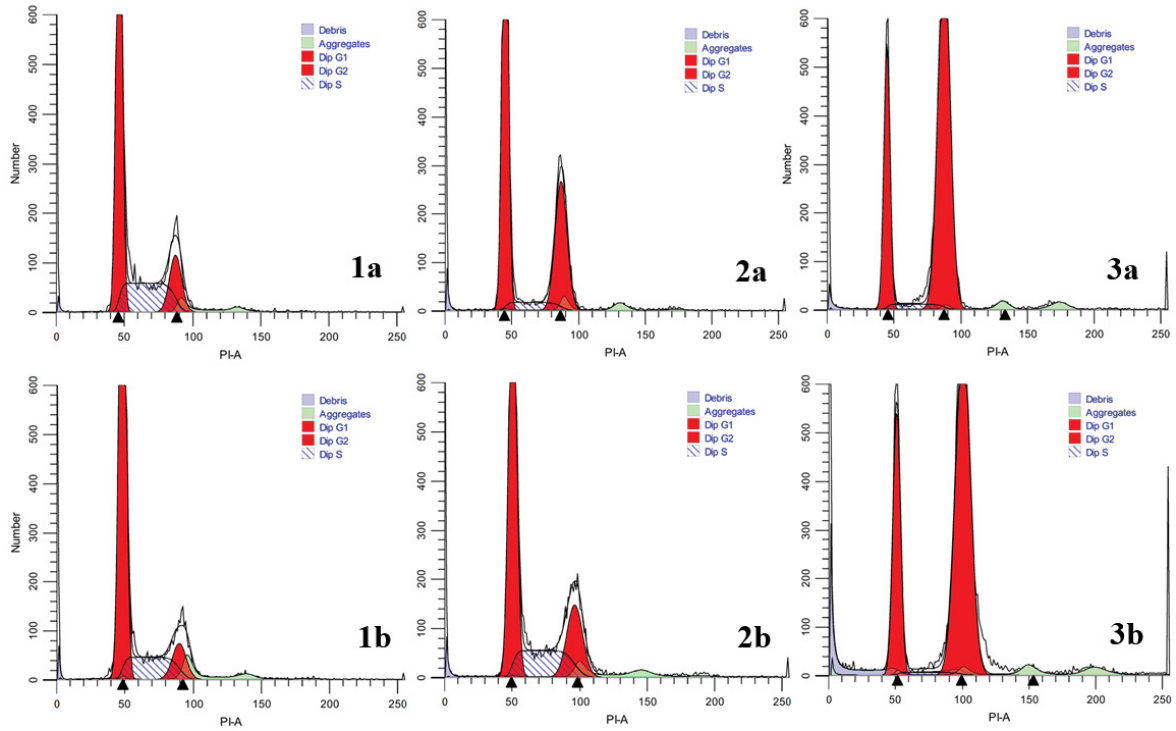

Figure 35. Flow cytometry histogram of experiment 1.
1a-3a: Control, 5 nM and 10 nM bortezomib 24 hours after treatment. 1b-3b: Control, 5 nM and 10 nM bortezomib 48 hours after treatment. The first peak in front corresponds to G1-phase and the second to G2-phase. The blue striped area between the peaks represents the SW-982 cells in synthesis phase.

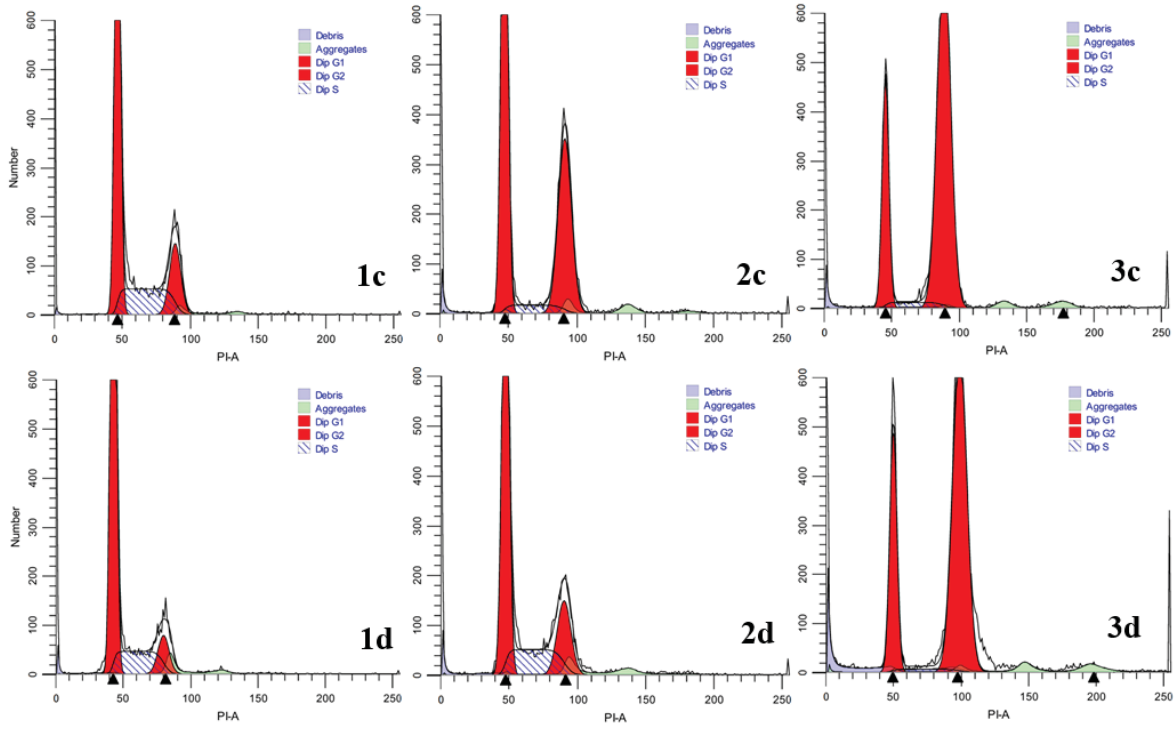

Figure 36. Flow cytometry histogram of experiment 2.
1c-3c: Control, 5 nM and 10 nM bortezomib 24 hours after treatment. 1d-3d: Control, 5 nM and 10 nM bortezomib 48 hours after treatment. The first peak in front corresponds to G1-phase and the second to G2-phase. The blue striped area between the peaks represents the SW-982 cells in synthesis phase.

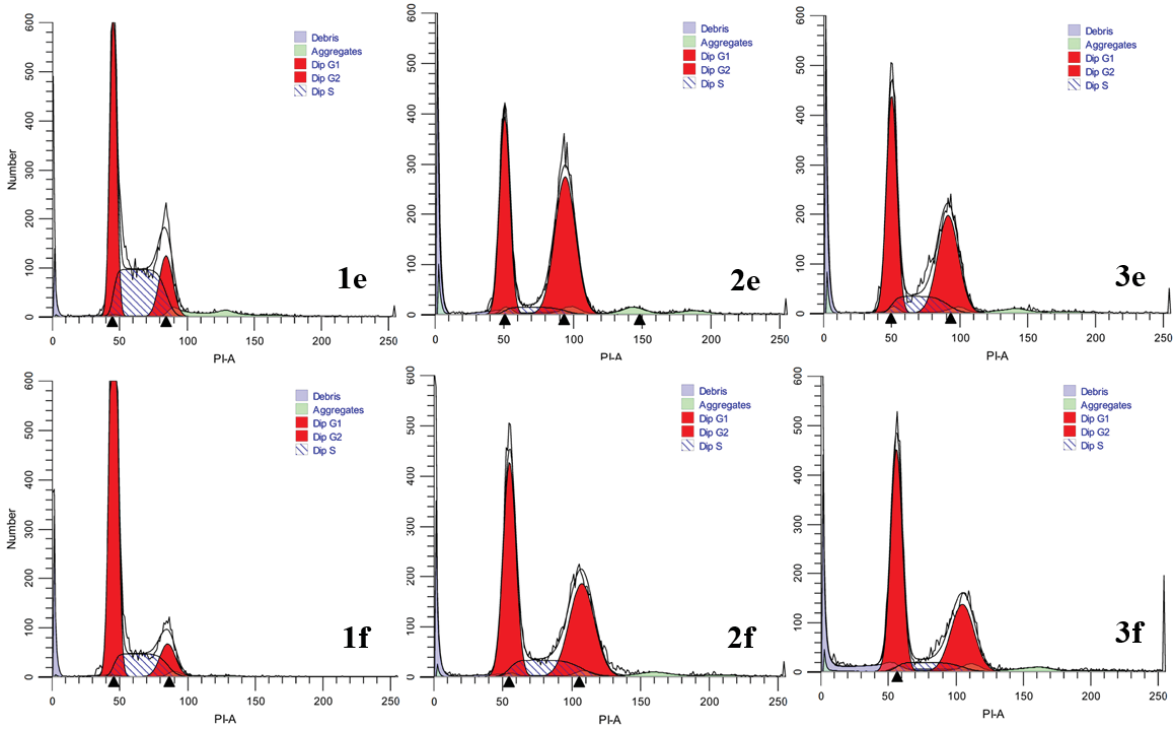

Figure 37. Flow cytometry histogram of experiment 3.
1e-3e: Control, 5 nM and 10 nM bortezomib 24 hours after treatment. 1f-3f: Control, 5 nM and 10 nM bortezomib 48 hours after treatment. The first peak in front corresponds to G1-phase and the second to G2-phase. The blue striped area between the peaks represents the SW-982 cells in synthesis phase.

The collected data is depicted summarized at the following bar graphs (Figures 38, 39).

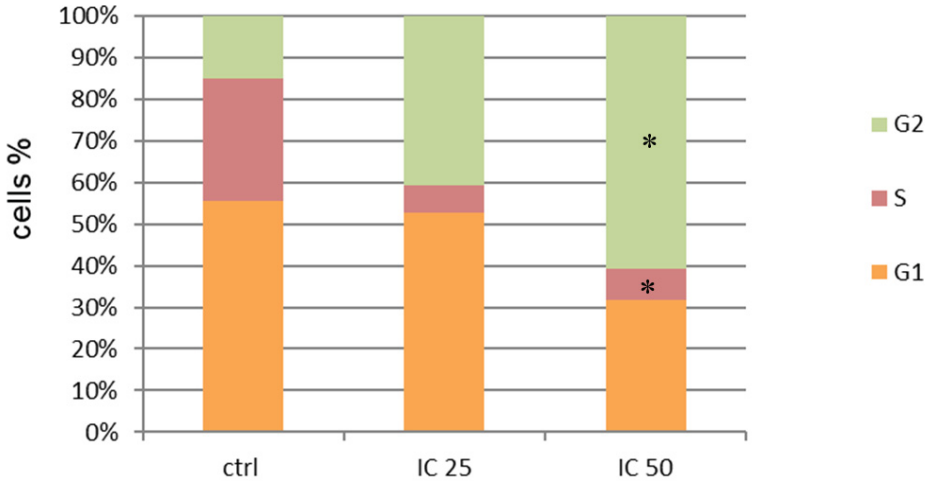

Figure 38. Summarized measurements (24 hours bortezomib exposure).
The highest accumulation of SW-982 cells in G2-phase appeared after the treatment with 10 nM Bortezomib (p=0,039)

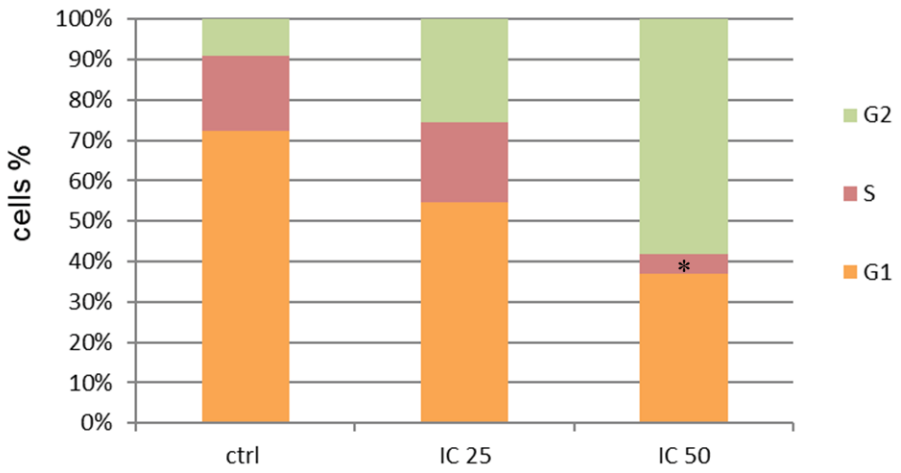

Figure 39. Summarized measurements (48 hours bortezomib exposure).
Both, the highest accumulation of cells in G2-phase and the lowest accumulation of cells in s-phase (p=0,032) appeared after the treatment with 10 nM Bortezomib.

4 Discussion

Synovial sarcomas (SSs) are rare soft tissue tumors (SST) showing aggressive behavior, a high recurrence rate and a strong tendency to form metastasis. Currently, surgical resection remains the only curative treatment. The approved cytotoxic therapies at present offer only limited benefits and a poor outcome. Therefore, if measures for local control are not curative, more targeted and less toxic therapeutic approaches are required.

The impact of the proteasome inhibitor bortezomib has already been tested on several malignancies. However, in the various group of sarcomas, the influence of bortezomib has only been tested on liposarcoma [67] as well as chondrosarcoma cells [68, 70]. Further, a recently published research paper from Perez M. and colleagues showed the efficacy of bortezomib on human sarcoma cells which inducing high levels of MAP17 [69]. The performed studies indicated that bortezomib reduces the viability of investigated sarcoma cells whereby the extent of cytotoxicity relies on the extent of proteasome inhibition [67].
In this study, we could observe similar effects on synovial sarcoma cells (SW-982 cell line).

Bortezomib clearly decreased cell proliferation and viability of SW-982 cells in a dose depended manner. Furthermore, cell viability assay showed a considerably less pronounced impact of bortezomib on not malign degenerated fibroblast-like synoviocytes (FLS). It should, however, be stated that in relation to FLS the measurements of real-time proliferation assay (xCelligence) did not reflect the results of cell viability assay. In fact, bortezomib decreased both cell index and viability at FLS. However, the impact on cell index (xCelligence) was considerably more pronounced compared to impact on cell viability. The deviation probably occurred because of the different systems behind these methods. Possibly FLS were still able to maintain metabolism after the monitored time period although they had already lost the adherence ability. Further studies are required to evaluate these findings.

The group around Kim JE suggested that bortezomib promotes G0/G1 arrest in cancer cells [71]. In 2017, also Bao X. and colleagues showed that in chondrosarcoma cells bortezomib downregulates cyclin D1 and therefore facilitates a G0/G1 phase arrest [70]. However, in contrast to the results of Kim JE [71] and Bao X [70] we found that in synovial sarcoma cells bortezomib notably induced a G2/M arrest in a dose dependent manner.
In addition to that we indicated a statistical significant decrease of CDK2 at IC_{50} after 48 hours (p=0,034). The cyclin A/CDK2-complex also phosphorylates a certain ubiquitin ligase (CDH1) and enables thereby progression through the G2/M check point by increasing the levels of cyclin B1 [72]. These facts may explain the observed G2/M arrest on the one hand and low CDK2 levels on the other. Contrary to that, expression levels of all investigated genes showed an increase at IC_{25}. However, it must be noted that only the data collected for CDK2 gene expression levels demonstrated statistical significance. Further studies are necessary to evaluate the gene expression levels under the influence of bortezomib and to clarify the reasons for these findings.

In 2016, Perez M. and colleagues proved evidence that patients with certain sarcomas may benefit from a treatment with bortezomib. The findings of the present study demonstrate that this may be valid also for patients suffering from certain SSs. A final statement cannot be made without further studies and more detailed investigations.

In summary, bortezomib showed an antineoplastic effect on synovial sarcoma cells in vitro. Our findings support bortezomib as a promising approach in considerations for new therapeutics in sarcoma therapy.

5 References

1. Mark DM, Michael SG, Bryan TJ, et al. Imaging of Synovial Sarcoma with Radiologic-Pathologic Correlation. Radio Graphics; 2006 Sep-Oct;26(5):1543-65.
2. Ghadially FN. Is synovial sarcoma a carcinosarcoma of connective tissue? Ultrastructural pathology;11(2-3);147-51.
3. Böcker W, Denk H, Heitz PhU, Moch H, editors. Pathologie. 4th ed. München: Urban & Fischer; 2008. p. 1104–1105.
4. Herzog CE. Overview of sarcomas in the adolescent and young adult population. Journal of Pediatric Hematology/oncology. 2005;27:215–8.
5. Deshmukh R, Mankin HJ, Singer S. Synovial sarcoma: the importance of size and location for survival. Clinical Orthopaedics and Related Research. 2004;419:155–161
6. Kransdorf MJ. Malignant soft-tissue tumors in a large referral population: distribution of diagnoses by age, sex, and location. AJR American Journal of Roentgenology. 1995;164:129–134
7. Eriksen C, Burns L, Bohlke A. Management of Monophasic Synovial Sarcoma of the Small Intestine. JSLS. 2010;14:421– 425.
8. Guillou L, Coindre JM, Bonichon F, et al. Comparative study of the National Cancer Institute and French Federation of Cancer Centers Sarcoma Group grading systems in a population of 410 adult patients with soft tissue sarcoma. Journal of Clinical Oncology. 1997;15:350–362.
9. Trassard M, Le Doussal V, Hacene K, et al. Prognostic factors in localized primary synovial sarcoma: A multicenter study of 128 adult patients. Journal of Clinical Oncology 2001;19:525–534.
10. Eilber FC, Dry MA. Diagnosis and Management of Synovial Sarcoma. Journal of Surgical Oncology 2008;97:314–320.
11. Ferrari A, Gronchi A, Casanova M, et al. Synovial sarcoma: a retrospective analysis of 271 patients of all ages treated at a single institution. Cancer 2004;101:627– 634.
12. Weiss SW, Goldblum JR. Malignant soft tissue tumors of uncertain type. In: Weiss SW, Goldblum JR, eds. Enzinger and Weiss's soft tissue tumors. 4th ed. St Louis, Mo: Mosby, 2001; 1483–1565

13. Lopez- Pousa A, Broto JM, Trufero JM, et al. SEOM Clinical Guideline of management of soft-tissue sarcoma (2016). Clinical & Translational Oncology 2016;18(12):1213–1220
14. Wu Y, Bi W, Han G, et al. Influence of neoadjuvant chemotherapy on prognosis of patients with synovial sarcoma. World Journal of Surgical Oncology. 2017;15: 101
15. PaulinoAC. Synovial sarcoma prognostic factors and patterns of failure. American Journal of Clinical Oncology 2004;27: 122–127.
16. Empfehlungen der Fachgesellschaft zur Diagnostik und Therapie hämatologischer und onkologischer Erkrankungen. Leitlinie: Weichgewebssarkome (Weichteilsarkome) des Erwachsenen. Juni 2017. Available at: https://www.onkopedia.com/de/onkopedia/guidelines/weichgewebssarkome-weichteilsarkome-des-erwachsenen/@@view/html/index.html#ID0EXUBG. Accessed August 14, 2008.
17. Smith AJ, Martin L. Do Cells Cycle? Proceedings of the National Academy of Sciences of the United States of America 1973 Apr;70(4): 1263–1267
18. Vermeulen K, Dirk R, Van Bockstaele, Berneman NZ. The cell cycle: a review of regulation, deregulation and therapeutic targets in cancer. Cell Prolif. 2003;36, 131–149
19. Pines J. Mitosis: a matter of getting rid of the right protein at the right time. Trends Cell Biol. 2006 Jan;16(1):55–63.
20. Heinrich CP, Müller M, Graeve L, editors. Löffler/Petrides Biochemie und Pathobiochemie. 9th ed. Berlin Heidelberg: Springer Medizin; 2014. p. 536.
21. Balasubramanian S, Tigges J, Toxavidis V, Marian H. Epithelial Cell Death Analysis of Cell Cycle by Flow Cytometry. In: Beckman Coulter Life. Available at: http://www.beckman.com/getattachment/9cbb570c-7b3b-4a69-86fb-a62302f1ea51/Epithelial%20Cell%20Death%20Analysis%20of%20Cell%20Cycle%20by%20Flow%20Cytometry. Accessed: October 10, 2016
22. Fischer M, Müller AG. Cell cycle transcription control: DREAM/MuvB and RB-E2F complexes. Crit Rev Biochem Mol Biol. 2017 Aug;11:1–25.
23. Malumbres M, Barbacid M. Cell cycle, CDKs and cancer: a changing paradigm. Nat Rev Cancer. 2009 Mar;9(3):153–66.
24. Kastan BM, Bartek J. Cell-cycle checkpoints and cancer. Nature. 2004 Nov 18;432(7015):316–23.

25. Lundberg AS, Weinberg RA. Functional inactivation of the retinoblastoma protein requires sequential modification by at least two distinct cyclin- cdk complexes. Mol Cell Biol. 1998 Feb;18(2):753–61.
26. Horn F, Moc I, Ziegler P, et al. Biochemie des Menschen. 6th edition. Stuttgart: Georg Thieme Verlag KG; 2015. p. 306.
27. Lew DJ, Kornbluth S. Regulatory roles of cyclin-dependent kinase phosphorylation in cell cycle control. Current Opinion in Cell Biology 1996;8:795–804
28. Bates S, Parry D, Bonetta L, et al. Absence of cyclin D/cdk complexes in cells lacking functional retinoblastoma protein. Oncogene. 1994 Jun;9(6):1633–40.
29. Oren M. Regulation of the p53 tumor suppressor protein. J Biol Chem. 1999 Dec 17;274(51):36031–4.
30. Budenholzer L, Cheng CL, Li Y, Hochstrasser M. Proteasome Structure and Assembly. Journal of Molecular Biology. 2017 Jun 3. Pii: S0022–2836(17)30270–X.
31. Ji CH, Kwon TY. Crosstalk and Interplay between the Ubiquitin-Proteasome System and Autophagy. Mol. Cells 2017;40(7):441–449.
32. Marteijn JAF, Jansen JH, Reijden BA. Ubiquitylation in normal and malignant hematopoiesis: novel therapeutic targets. Leukemia. 2006 Sep;20(9):1511–8.
33. Yang H, Zonder AJ, Dou QP. Clinical development of novel proteasome inhibitors for cancer treatment. Expert Opin Investig Drugs. 2009 July;18(7): 957–971.
34. Kouroukis TC, Baldassarre FG, Haynes AE, et al. Bortezomib in multiple myeloma: systematic review and clinical considerations. Curr Oncol. 2014 Aug;21(4):e573–e603.
35. European Medicines Agency. What is Bortezomib Accord and what is it used for? Available at: http://www.ema.europa.eu/ema/index.jsp?curl=pages/medicines/human/medicines/003984/human_med_001882.jsp&mid=WC0b01ac058001d124. Accessed: July 28, 2017.
36. Ludwig H, Khayat D, Giaccone G, Falcon T. Proteasome Inhibition and Its Clinical Prospects in the Treatment of Hematologic and Solid Malignancies. Cancer. 2005 Nov 1;104(9):1794–807.
37. Kao C, Chao A, Tsai LC, et al. Bortezomib enhances cancer cell death by blocking the autophagic flux through stimulating ERK phosphorylation. Cell Death Dis. 2014 Nov 6;5:e1510.

38. Munoz-Galvan S, Gutierrez G, Perez M, Carnero A. MAP17 (PDZKIP1) Expression Determines Sensitivity to the Proteasomal Inhibitor Bortezomib by Preventing Cytoprotective Autophagy and NFkB Activation in Breast Cancer. Mol Cancer Ther. 2015 Jun;14(6):1454–65.
39. Almond JB, Cohen GM. The proteasome: a novel target for cancer chemotherapy. Leukemia. 2002 Apr;16(4):433–43.
40. ATCC: The Global Bioresource Center. SW 982 [SW-982, SW982] (ATCC® HTB-93™). Available at: https://www.lgcstandards-atcc.org/products/all/HTB-93.aspx?geo_country=at. Accessed: July 12, 2017.
41. Butler JM. Short tandem repeat typing technologies used in human identity testing. Biotechniques. 2007 Oct;43(4):ii–v.
42. Hohoff C, Brinkmann B. Human identity testing with PCR-based systems. Mol Biotechnol. 1999 Dec 1;13(2):123–36.
43. Collins PJ, Hennessy LK, Leibelt CS, et al. Developmental validation of a single-tube amplification of the 13 CODIS STR loci, D2S1338, D19S433, and amelogenin: the AmpFlSTR Identifiler PCR Amplification Kit. J Forensic Sci. 2004 Nov;49(6):1265–77.
44. Herrmann H, Aebi U. Intermediate filaments and their associates: multi-talented structural elements specifying cytoarchitecture and cytodynamics. Curr Opin Cell Biol 2000;12:79–90.
45. Satelli A, Li S. Vimentin in cancer and its potential as a molecular target for cancer therapy. Cell Mol Life Sci. 2011 Sep;68(18):3033–46.
46. Challa AA, Stefanovic B. A novel role of vimentin filaments: binding and stabilization of collagen mRNAs. Mol Cell Biol. 2011 Sep;31(18):3773–89.
47. Berridge MV, Tan AS. Characterization of the cellular reduction of 3-(4,5-dimethylthiazol-2-yl)-2,5-diphenyltetrazolium bromide (MTT): Subcellular localization, substrate dependence, and involvement of mitochondrial electron transport in MTT reduction. Arch Biochem Biophys. 1993 Jun;303(2):474–82.
48. Promega, Technical Bulletin. CellTiter 96® AQ_{ueous} OneSolution Cell Proliferation Assay. Available at: https://at.promega.com/-/media/files/resources/protocols/technical-bulletins/0/celltiter-96-aqueous-one-solution-cell-proliferation-assay-system-protocol.pdf. Accessed: August 10, 2017.
49. ACEA Biosciences Inc.. RTCA iCELLigence. Available at: https://www.aceabio.com/products/icelligence/. Accessed: August 12, 2017.

50. NCBI. Polymerase Chain Reaction (PCR). Available at: https://www.ncbi.nlm.nih.gov/probe/docs/techpcr/. Accessed: August 29, 2017.
51. Bio-Rad. What is Real-Time PCR (qPCR)?. Available at: https://www.bio-rad.com/de-at/applications-technologies/what-real-time-pcr-qpcr. Accessed: August 12, 2017.
52. Gill P, Amir G. Acid Isothermal Amplification Technologies. Nucleosides Nucleotides Nucleic Acids. 2008 Mar;27(3):224–43.
53. LibreTexts. Cloning and Genetic Engineering. Available at: https://bio.libretexts.org/TextMaps/Map%3A_Concepts_in_Biology_(OpenStax)/10%3A_Biotechnology/10.1%3A_Cloning_and_Genetic_Engineering. Accessed: September 01, 2017.
54. Lui C, Cady CN, Batt AC. Nucleic Acid-based Detection of Bacterial Pathogens Using Integrated Microfluidic Platform Systems. Sensors (Basel). 2009;9(5):3713–44.
55. The Scientist. How it Works: Real Time PCR. Available at: http://www.the-scientist.com/?articles.view/articleNo/24568/title/How-it-Works--Real-Time-PCR/. Accessed: September 05, 2017.
56. Qiagen. RNeasy Mini Handbook. Available at: https://www.qiagen.com/fr/resources/resourcedetail?id=14e7cf6e-521a-4cf7-8cbc-bf9f6fa33e24&lang=en. Accessed: September 05, 2017.
57. Thermo Scientific. NanoDrop 1000 Spectrophotometer V3.8 User's Manual. Available at: https://tools.thermofisher.com/content/sfs/manuals/nd-1000-v3.8-users-manual-8%205x11.pdf. Accessed: September 07, 2017.
58. Agilent Technologies. Agilent 2100 Bioanalyzer 2100 Expert User's Guide. Available at: http://www.agilent.com/cs/library/usermanuals/Public/G2946-90004_Vespucci_UG_eBook_(NoSecPack).pdf. Accessed: September 10, 2017.
59. Schroeder A, Mueller O, Stocker S, et al. The RIN: an RNA integrity number for assigning integrity values to RNA measurements. BMC Mol Biol. 2006 Jan 31;7:3.
60. Thermo Fisher Scientific. DNase I, RNase-free. Available at: https://www.thermofisher.com/order/catalog/product/EN0525. Accessed: September 10, 2017.

61. Thermo Fisher Scientific. Product Information DNase I, RNase-free. Available at: https://assets.thermofisher.com/TFS-Assets/LSG/manuals/MAN0012000_DNase_I_RNasefree_1UuL_UG.pdf. Accessed: September 11, 2017.
62. BioRad. SsoAdvanced™ Universal SYBR® Green Supermix. Available at: http://www.bio-rad.com/webroot/web/pdf/lsr/literature/10031339.pdf. Accessed: September 11, 2017.
63. Qiagen. QIAamp® DNA Mini and Blood Mini Handbook. Available at: https://www.qiagen.com/ch/resources/resourcedetail?id=62a200d6-faf4-469b-b50f-2b59cf738962&lang=en. Accessed: September 11, 2017.
64. Semrock. Filters for Flow Cytometry. Available at: https://www.semrock.com/flow-cytometry.aspx. Accessed: September 12, 2017.
65. Sigma- Aldrich. Propidium iodide. Available at: http://www.sigmaaldrich.com/catalog/product/sigma/p4170?lang=de&region=AT. Accessed: September 13, 2017.
66. R&D Systems. Flow Cytometry Protocol for Analysis of Cell Viability using Propidium Iodide. Available at: https://www.rndsystems.com/resources/protocols/flow-cytometry-protocol-analysis-cell-viability-using-propidium-iodide. Accessed: September 13, 2017.
67. Hu Y, Wang L, Wang L, et al. Preferential cytotoxicity of bortezomib to ward highly Malignant human liposarcoma cells via suppression of MDR1 expression and function.Toxicol Appl Pharmacol 2015; 283(1):1±8.
68. Lohberger B, Steinecker-Frohnwieser B, Stuendl N, et al. The Proteasome Inhibitor Bortezomib Affects Chondrosarcoma Cells via the Mitochondria-Caspase Dependent Pathway and Enhances Death Receptor Expression and Autophagy. PLoS One. 2016 Dec 15;11(12):e0168193.
69. Perez M, Peinado-Serrano J, Garcia-Heredia MJ, et al. Efficacy of bortezomib in sarcomas with high levels of MAP17 (PDZK1IP1). Oncotarget. 2016 Oct 11;7(41):67033–67046.
70. Bao X, Ren T, Huang Y, et al. Bortezomib induces apoptosis and suppresses cell growth and metastasis by inactivation of Stat3 signaling in chondrosarcoma. Int J Oncol. 2017 Feb;50(2):477-486.

71. Kim JE, Lee JI, Jin DH, et al. Sequential treatment of HPV E6 and E7-expressing TC-1 cells with bortezomib and celecoxib promotes apoptosis through p-p38 MAPK-mediated downregulation of cyclin D1 and CDK2. Oncol Rep. 2014 May;31(5):2429-37.

72 Ortega S, Prieto I, Odajima J, et al. Cyclin-dependent kinase 2 is essential for meiosis but not for mitotic cell division in mice. Nat Genet. 2003 Sep;35(1):25-31.